



HAL
open science

Flow of the partially molten crust in the Variscan foreland revealed by U–Th–Pb dating of metamorphism, magmatism and deformation (Agly Massif, Eastern Pyrenees)

J. Vanardois, P. Trap, F. Roger, P. Goncalves, D. Marquer, J. Paquette, G. Siron, Thierry Baudin

► To cite this version:

J. Vanardois, P. Trap, F. Roger, P. Goncalves, D. Marquer, et al.. Flow of the partially molten crust in the Variscan foreland revealed by U–Th–Pb dating of metamorphism, magmatism and deformation (Agly Massif, Eastern Pyrenees). *International Journal of Earth Sciences*, In press, 10.1007/s00531-022-02229-7. hal-03771501

HAL Id: hal-03771501

<https://hal.umontpellier.fr/hal-03771501>

Submitted on 7 Sep 2022

HAL is a multi-disciplinary open access archive for the deposit and dissemination of scientific research documents, whether they are published or not. The documents may come from teaching and research institutions in France or abroad, or from public or private research centers.

L'archive ouverte pluridisciplinaire **HAL**, est destinée au dépôt et à la diffusion de documents scientifiques de niveau recherche, publiés ou non, émanant des établissements d'enseignement et de recherche français ou étrangers, des laboratoires publics ou privés.

[Click here to view linked References](#)

1 ***Flow of the partially molten crust in the Variscan foreland revealed by U-Th-Pb dating of***
2 ***metamorphism, magmatism and deformation (Agly Massif, eastern Pyrenees).***

3 Vanardois^{1*} J., Trap¹ P., Roger² F., Goncalves¹ P., Marquer¹ D., Paquette³ JL., Siron⁴ G., Baudin⁵ T.

4 jonas.vanardois@univ-fcomte.fr; pierre.trap@univ-fcomte.fr; francoise.roger@umontpellier.fr;

5 philippe.goncalves@univ-fcomte.fr; didier.marquer@univ-fcomte.fr; [6 \[bpclermont.fr\]\(mailto:bpclermont.fr\); \[siron@wisc.edu\]\(mailto:siron@wisc.edu\) ; \[t.baudin@brgm.fr\]\(mailto:t.baudin@brgm.fr\)](mailto:j.l.paquette@opgc.univ-</p></div><div data-bbox=)

7 ¹UMR 6249 Chrono-environnement, Université de Bourgogne-Franche-Comté, 25030 Besançon,
8 France.

9 ²Géosciences Montpellier, Campus Triolet, Université Montpellier, CNRS, 34095 Montpellier Cedex
10 5, France.

11 ³Laboratoire Magmas et Volcans (CNRS-UMR 6524), Campus Universitaire des Cézeaux, 63178
12 Aubière Cedex, France.

13 ⁴WiscSIMS Laboratory, University of Wisconsin-Madison, Madison, Wisconsin 53706, United States
14 of America.

15 ⁵BRGM-French Geological Survey, 3 Avenue Claude Guillemin, 45100, Orléans, France.

16

17 *Corresponding author: jonasvanardois@gmail.com +33(0)606755562; Present address: 16 route de
18 Gray, 25030 Besançon.

19

20 **Keywords:** Crustal flow, Strain partitioning Variscan orogen, Agly Massif, LA-ICPMS U-Th-Pb dating

21

22 **Abstract**

23 In this contribution, we investigate the spatial and temporal evolution of mid-crustal flow in the Agly
24 massif (North Pyrenean Zone) that represents the southern foreland of the Variscan orogenic plateau.
25 In the Agly massif, the middle crust is represented by an Ediacarian-Devonian series of
26 metasedimentary rocks that recorded high-grade metamorphism synchronously with crustal thinning
27 (D2) and dextral wrenching (D3) during Carboniferous. D2 crustal thinning formed a penetrative S2
28 flat-lying foliation and localized C2 extensional shear zones with a top-to-the-North kinematics. D2
29 planar fabrics are deformed by a D3 dextral transpression localized into a two-kilometers wide high-
30 strain zone. We performed LA-ICPMS U-Th-Pb dating on zircon and monazite from small magmatic
31 bodies and from metamorphic rocks showing strain features relative to D2 and/or D3. Our results,
32 compiled with published data, argue that the middle crust of the Agly massif reached high-temperature
33 and suprasolidus conditions at ca. 325-320 Ma and was partially molten until ca. 300 Ma. They also
34 indicate that the D2 thinning and top-to-the north shearing was active from ca. 325 to 290 Ma. D2
35 extension and D3 transpression were synchronous from ca. 308 to 290 Ma. Making a comparison with
36 the Pyrenean Axial Zone, the Montagne Noire and the French Central massif, we propose a two-step
37 tectonic model for the mid-crustal flow with a horizontal flow towards South in both the orogenic
38 plateau and the southern forelands between ca. 325 and 310 Ma and locally reoriented into an E-W
39 longitudinal flow between 310 and 300 Ma in high-strain dextral strike-slip shearing domains.

40 **Introduction**

41 The Variscan belt is considered as an ancient analogue of large and hot orogens (e.g. Maierova et al.
42 2016). As such, it constitutes a natural laboratory to observe deep crustal flow mechanisms (e.g.
43 Schulmann et al. 2008), as those currently operating beneath the Andean (e.g. Gerbault et al. 2005) and
44 Tibetan orogenic plateau (e.g. Clark and Royden 2000). In the French Variscan belt, the occurrence of
45 eclogite boudins hosted in migmatites exhumed in the foreland has been interpreted as an evidence for
46 southward horizontal flow of the partially molten lower crust (Fig. 1, Whitney et al. 2015, Pitra et al.
47 2021). In the eastern part of the French Massif Central, the southward rejuvenation of partial melting

48 and the progressive evolution of crustal-derived plutonic rocks from ca. 345 Ma to ca. 310 Ma (Laurent
49 et al. 2017) is attributed to a southward horizontal growth of the Variscan belt and formation of an
50 orogenic plateau by gravity-driven lateral flow of the partially molten orogenic root (Vanderhaeghe et
51 al. 2020).. Later structures are dominantly interpreted as a late-orogenic gravitational collapse recorded
52 between 305 and 290 Ma (e.g. Rey et al. 2011, 2017; Vanderhaeghe et al. 2020 and references therein).

53 In addition, the Carboniferous building of the Variscan belt was widely impacted by the development
54 of crustal-scale strike-slip shear zones (e.g. Carreras and Druguet 2014; Franke et al. 2017; Chardon et
55 al. 2020; Edel et al. 2018 and references therein). It is far from being clear to what extent the gravity-
56 driven lateral flow and the strike-slip-controlled longitudinal or extrusional flow interacted in the
57 partially molten orogenic root. Accurate dating of melting and solid-state deformation, as well as
58 characterization of feedback relationship between plutonism and crustal-scale shear zones are still
59 needed to understand the flow dynamics of partially molten crust.

60 The North-Pyrenean-Zone (NPZ, Fig. 1) represents the southern foreland of the Variscan belt where the
61 partially molten orogenic root might have flowed southwards (Whitney et al. 2015; Vanderhaeghe et
62 al. 2020). In comparison with the hinterland areas, the NPZ still lacks precise geochronological data
63 that are required to date deformation and fully understand the flow pattern of the partially molten crust
64 in the external portion of the Variscan orogenic plateau. At the eastern edge of the NPZ, the Agly massif
65 shows a finite strain pattern that results from the superposition of flat-lying and vertical foliations related
66 to bulk thinning and dextral wrenching, respectively. Based on U-Th-Pb zircon dating of plutons
67 (Olivier et al. 2004, 2008; Tournaire Guille et al. 2019) and their relationships with the deformation
68 phases, Vanardois et al. (2020) proposed that the flat-lying structure (D2) and wrench-related vertical
69 structures (D3) may have been partially coeval. In this contribution, we performed LA-ICPMS U-Th-
70 Pb dating on zircon and monazite from pegmatites, leucogranites and metamorphic rocks (i.e.
71 orthogneiss and paragneiss) in order to constrain the timing of D2 thinning and D3 wrenching, and
72 associated metamorphism and magmatism. These new geochronological results compared with
73 structural and metamorphic data allow us to discuss the strain partitioning evolution in space and time
74 during middle crustal flow of the Variscan belt foreland.

75 **Geological Setting**

76 The Variscan Pyrenees are located in the external domain of the Variscan belt and represent its southern
77 orogenic foreland (Druguet 2001; Edel et al. 2018; Laurent et al. 2017; Aguilar et al. 2013; Martinez-
78 Catalan et al., 2021) (Fig. 1a). The Pyrenean Axial Zone (PAZ) and the North Pyrenean Zone (NPZ)
79 are separated by the EW-striking North Pyrenean Fault (NPF). These two zones consist of Proterozoic
80 to Paleozoic sedimentary rocks deformed and metamorphosed between the middle Carboniferous and
81 the early Permian (Mezger and Gerdes 2016; Denèle et al. 2014; Aguilar et al. 2013; Schnapperelle et
82 al. 2020; Vacherat et al. 2017; Cochelin et al. 2021; Cugerone et al. 2021; Vielzeuf et al. 2021). In both
83 PAZ and NPZ, the Variscan orogeny is associated with a widespread Carboniferous to Permian
84 magmatism (e.g. Denèle et al. 2014; Pereira et al. 2014; Druguet et al. 2014; Lemirre 2016; Vacherat
85 et al. 2017; Lemirre et al. 2019).

86 In the NPZ, few relics of kyanite have been described (Fonteilles et al. 1964; Fonteilles 1970; Fonteilles
87 and Guitard 1971) leading some authors to propose an early thickening event (D1) related to nappe
88 stacking (e.g. Bouhallier et al. 1991; Olivier et al. 2004). LA-ICPMS U-Th-Pb ages at ca. 325-320 Ma
89 obtained in the NPZ are interpreted as the onset of partial melting during D1 prior to the pervasive high
90 temperature and low-pressure event (M2) widely recorded in the Pyrenees (Lemirre 2016). This high
91 temperature event is coeval with the widespread development of sub-horizontal foliation, interpreted as
92 the result of extensional collapse (D2) during late Carboniferous (Bouhallier et al. 1991; de Saint-
93 Blanquat 1993; Vanardois et al. 2020).

94 At the eastern edge of the NPZ, the Agly massif forms a WNW-ESE trending, 30 km long and 10 km
95 wide Variscan massif that was exhumed during Cretaceous extension and subsequent Tertiary Pyrenean
96 continental collision. The Agly massif is composed of a Proterozoic to Devonian metasedimentary
97 sequence (Fonteilles 1970; Berger et al. 1993) that contains sills of Cambrian (ca. 540 Ma) and
98 Ordovician (ca. 450 Ma) orthogneisses (Tournaire Guille et al. 2019; Paquette et al. 2021).

99 The metasedimentary sequence is classically subdivided into an infrastructure and a suprastructure
100 (Fonteilles 1970). The suprastructure consists of unmolten metasedimentary rocks represented by

101 Cambrian to Ordovician micaschists and schists, Silurian black-schists and Devonian marbles (Fig. 2)
102 with few metric quartzite layers. The suprastructure is characterized by a HT-LP metamorphic gradient
103 of $\sim 55^{\circ}\text{C}/\text{km}$ (Vielzeuf 1984; Andrieux 1982a, 1982b; Delay 1989; Bouhallier et al. 1991; Siron et al.
104 2020) with a maximum temperature of 680°C at its base (Siron et al. 2020; Bouhallier et al. 1991; Delay
105 1989). The infrastructure is composed of partially molten metapelites, metagreywackes, calc-
106 silicates, marbles and meta-igneous rocks, the latter being mainly orthogneissified (Fig. 2). Siron et al.
107 (2020) have shown that the infrastructure is characterized by a near isothermal gradient buffered at
108 around $740\text{-}790^{\circ}\text{C}$ between 0.5 and 0.66 GPa. LA-ICPMS U-Th-Pb monazite dating of two high-
109 aluminium pelitic samples (kinzigites) estimated the peak of the HT-LP metamorphism at ca. 305 Ma
110 (Siron et al. 2020). Several 100-meter thick, flat-lying mylonitic shear zones are documented in the
111 infrastructure, together with the main Caladroy shear zone (CSZ) that is located near the anatectic front
112 (Delay et al. 1989; Bouhallier et al. 1991; Siron et al. 2020; Vanardois et al. 2020) (Fig. 3a). The CSZ
113 separates the infra- and suprastructure (Vanardois et al. 2020) and subtracted about 5 km of crustal
114 material (Delay 1989; Bouhallier et al. 1991; Siron et al. 2020).

115 Several Carboniferous magmatic rocks intruded at different levels into the infra- and supra-structures.
116 The Ansignan pluton is a 500 meter-thick charnockitic laccolith emplaced in the deepest part of the
117 infrastructure, with smaller satellite sills observed in the southern part of the massif (Fig. 2) (Delay
118 1989; Fonteilles et al. 1993). The Ansignan pluton is concordant with the layering of the surrounding
119 migmatitic gneisses (Althoff et al., 1994; Vanardois et al. 2020) and consists of three facies: (i) a
120 melanocratic K-feldspar porphyric, garnet and orthopyroxene-bearing granodiorite, (ii) a garnet-bearing
121 leucogranite and (iii) mafic enclaves (Berger et al. 1993; Delay 1989; Althoff et al. 1994; Olivier et al.
122 2008). These three facies have been dated by U-Pb method by ID-TIMS on zircon and monazite and
123 yielded ages between 315 and 290 Ma (Postaire 1982; Respaut and Lancelot 1983). The most recent
124 age at 307 ± 3 Ma (U-Th-Pb LA-ICPMS on zircon) was interpreted by Tournaire Guille et al. (2019) as
125 the emplacement age of the Ansignan charnockite. However, these same authors also obtained on a
126 mylonitized charnockitic sill two concordia ages, one at 313.9 ± 2.9 Ma on zircon cores and the other
127 at 298.6 ± 2.7 Ma on zircon rims, without really interpreting them. The Cassagnes granite occurs as a

128 set of few meter-thick sills in the infrastructure located, near the Cassagnes village (Fig. 2). It is a
129 melanocratic K-feldspar phenocrysts, garnet-bearing granodiorite, very similar to the Ansignan
130 charnockite except that orthopyroxene is rare, and it was emplaced at 308 ± 3 Ma (U-Pb LA-ICPMS on
131 zircon; Tournaire et al. 2019). The emplacement of a monzogranitic sill into the infrastructure has been
132 dated by upper intercept at 317 ± 3 Ma (ID-TIMS on zircon; Olivier et al. 2004), but a few years later
133 Olivier et al. (2008) interpreted this age as a mixing date between inherited cores and Variscan rims.

134 The suprastructure is intruded by the Tournefort diorite and the Saint-Arnac pluton (Fig. 2). The
135 Tournefort diorite has been dated by upper intercept at 308 ± 1 Ma and by a concordia age at 307 ± 1
136 Ma (ID-TIMS on zircon; Olivier et al. 2004, 2008). The southern part of the Saint-Arnac pluton is
137 composed of several granitic facies partly mingled with dioritic facies that may be cogenetic with the
138 Tournefort diorite (Olivier et al. 2008). On the southern edge of the Saint-Arnac pluton, the age of the
139 granodiorite has been dated by upper intercept at 304 ± 5 Ma (ID-TIMS on zircon; Olivier et al. 2008)
140 and by weighted mean $^{206}\text{Pb}/^{238}\text{U}$ dates at $308 \pm 4/-2$ Ma (LA-ICPMS on zircon; Odlum and Stockli
141 2019), whereas the zircons from the northern edge of the pluton yield a mean $^{206}\text{Pb}/^{238}\text{U}$ age of $301 \pm 3/-$
142 2 Ma (LA-ICPMS; Odlum and Stockli 2019). Numerous meter-sized pegmatitic and leucogranitic
143 dykes and sills intruded the infra- and supra-structures and the plutons.

144 The main penetrative strain pattern is related to the D2 deformation event defined by a pervasive flat-
145 lying foliation S2 (Vanardois et al. 2020). D2 reworked an early vertical N-S trending foliation
146 attributed to the D1 thickening event (Fig. 3 and 4a-b, Vanardois et al. 2020). The D2 deformation was
147 coeval with the HT/LP M2 metamorphism, migmatization, and the Ansignan and Cassagnes intrusions
148 (Delay 1989; Paquet and Mansy 1991; Bouhallier et al. 1991; Althoff et al. 1994, Vanardois et al. 2020).
149 D2 deformation continued during retrogressed conditions and formed C2 extensional shear zones (Fig.
150 3 and 4c-d) responsible for the bulk thinning of the Agly massif. The Caladroy shear zone (CSZ),
151 separating the infra- and suprastructure, is one of these C2 shear zones (Fig. 3). The evolution of D2
152 from suprasolidus S2 foliations to subsolidus C2 strain localization (Vanardois et al., 2020) is defined
153 in the following sections as S2 and C2 structures, respectively. Siron et al. (2020) documented LA-

154 ICPMS U-Th-Pb ages at ca. 296-300 Ma from monazite overgrowths of a C2 mylonite, interpreted as
155 the timing of late D2 crustal thinning.

156 In the northern part of the Agly massif, Vanardois et al. (2020) described a third deformation phase D3
157 corresponding to a dextral transpression localized along an E-W 2 km-wide corridor (Fig. 3 TDZ). This
158 D3 corridor shows a prominent vertical foliation S3 that reworked former D2 (S2 and C2) planar fabrics
159 (Fig. 3 and 4e-f). The D3 event is subdivided into an early transtensional deformation, named proto-D3
160 and a late transpressional regime D3 *sensu stricto*, named Late-D3 (Vanardois et al. 2020). The D3
161 corridor acted as preferential pathways for upward migration of the Tournefort diorite and Saint-Arnac
162 granite magmas (Vanardois et al. 2020).

163 The Tertiary Pyrenean tectonics is characterized in the Agly massif by brittle deformation with steep
164 reversed faults affecting the Variscan basement and Mesozoic rocks. This last stage is affected by N020
165 and N150 striking conjugate strike-slip faults accommodating the N-S Pyrenean compression.

166 **U-Th-Pb geochronology**

167 In this study, we report new zircon and monazite U-Th-Pb dates from nine rock samples from the Agly
168 massif corresponding to syn-tectonic granitoids or mylonitic rocks have been collected with respect to
169 the main deformation events and their location in the infra- or suprastructure (Fig. 2 and 3 and Table 1
170 for locations). (i) Samples Ag57 and Ag3B are located in S2 strain domains. Sample Ag57 is an
171 undeformed leucogranitic sill located in the western part of the Agly massif in the deepest part of the
172 infrastructure. The sample Ag3B is a migmatitic paragneiss located in the upper part of the
173 infrastructure, (ii) Samples Ag38, Ag03 and Ag47 are pegmatites located within the C2 shear zones.
174 Two of them are located within the CSZ at the infra- and suprastructure boundary, one pegmatite is
175 deformed (Ag38), the other is slightly deformed (Ag03). The pegmatite Ag47 is located in the
176 suprastructure and is mylonitized by a C2 shear zone. (iii) Samples Ag08 and Ag06 are two dykes that
177 crosscut the Proto-D3 transtensional structures from the Tournefort area. One is a pegmatite located in
178 the Tournefort diorite (Ag08), the other is a leucogranite emplaced near the Saint-Arnac pluton (Ag06).
179 (iv) Sample Ag48 is a migmatitic orthogneiss from the infrastructure located in the Late-D3

180 transpressional structures of the D3 corridor while Ag51 is a leucogranite collected within the axial
181 plane of a late-D3 fold at the vicinity of the D3 corridor. Samples presentations are detailed in the
182 followings.

183

184 **Analytical method**

185 Monazite and zircon were obtained by standard crushing and heavy liquid and magnetic separation
186 using Frantz isodynamic techniques. The crystals were handpicked under a binocular microscope, then
187 mounted in epoxy resin discs and polished to expose mid-grain sections. One exception is monazite
188 from sample Ag3B that was analysed in-situ (thin section) to preserve textural relationships, the rock-
189 forming mineralogical assemblage and the fabrics. Cathodoluminescence (CL) and backscattered
190 electrons (BSE) images were used to select points for analysis (Fig. S1 and S2, supplementary material).
191 U-Th-Pb geochronology of zircon and monazite was obtained by laser ablation inductively coupled
192 plasma spectrometry (LA-ICPMS) at the Laboratoire Magmas et Volcans (Clermont-Ferrand, France).
193 The analysis involved the ablation of minerals with a Resonetics Resolution M-50 powered by an ultra-
194 short pulse ATL Atlex Excimer laser system operating at a wavelength of 193 nm. For zircon and
195 monazite, spot diameters of 27 μm or 33 μm and 12 μm were used, associated with repetition rates of 3
196 Hz and 1 Hz, and laser fluences of 4J/cm² and 9J/cm² respectively. The ablated material was carried
197 by helium and then mixed with nitrogen and argon before injection into the plasma source of an Agilent
198 7500 cs ICP-MS equipped with a dual pumping system to enhance sensitivity (Paquette et al. 2014).
199 The detailed analytical procedures are described in Paquette and Tiepolo (2007), Hurai et al. (2010),
200 Paquette et al. (2014) and in the supplementary material (Table S1). Data reduction was carried out with
201 the GLITTER® software package from Macquarie Research Ltd (Van Achterbergh et al. 2001).
202 Calculated ratios were exported and ages and diagrams were generated using Isoplot/Ex v. 2.49 software
203 package of Ludwig (2001). In the text and figures, all uncertainties in ages are given at the $\pm 2\sigma$ level.
204 The decay constants used for the U-Th-Pb system are those determined by Jaffey et al. (1971) and
205 recommended by IUGS (Steiger and Jäger 1977). Analytical results are given in Tables S2 and S3

206 (supplementary material). Monazite data by LA-ICPMS were plotted in a U-Th-Pb modified concordia
207 diagram ($^{206}\text{Pb}/^{238}\text{U}$ vs $^{208}\text{Pb}/^{232}\text{Th}$) because ^{232}Th measurement is more accurate than ^{235}U .

208 **Samples from S2 strain domains**

209 *The Vivier deformed leucogranite (Ag57)*

210 The Vivier leucogranite (Ag57) is a two-meter-thick magmatic sill composed of Qtz + Kfs + Pl \pm Grt
211 \pm Bt. The sill is sub-horizontal, undeformed and parallel with the surrounding S2 foliation. Most of the
212 analysed monazite crystals in sample Ag57 are round-shaped, translucent to slightly opaque and yellow.
213 BSE images of some monazite grains show a simple growth zoning (Fig. S1). Twenty-nine analyses
214 were performed on nineteen monazite crystals (Fig. 5a; Table S2). Unlike Pb concentrations (1356-
215 2152 ppm), Th and U contents vary significantly between different crystals or different domains within
216 a single crystal. Th and U contents range from 18394 to 75616 ppm and 1847 to 11425 ppm,
217 respectively. Th/U ratios are between 1.6 and 33.5 (Table S2). All these data are concordant between
218 280 and 320 Ma and, excluding two analyses (dotted ellipses), yield a concordia age of 298.9 ± 1.9 Ma
219 ($\text{MSWD}_{(\text{C+E})} = 1.7$; $n = 26$) (Fig. 5a).

220 The analysed zircon crystals are transparent, colourless and slightly rounded. CL imaging shows
221 complex internal textures with the systematic occurrence of inherited core displaying either a typical
222 magmatic concentric oscillatory zoning or patchy zoning textures surrounded by rims (Fig. S2). Forty-
223 five analyses were performed on thirty zircon grains (Table S3). Among these data, thirty-seven are
224 concordant but scattered along the concordia curve between around 700 to 300 Ma and form two distinct
225 clusters: a scattered population between 700 and 450 Ma (group 1) and a range of dates between 350
226 and 300 Ma (group 2) (Fig. 5b; Table S3). The single-analysis concordia ages histogram suggests that
227 the group 1 data are distributed among at least two main populations, one at 630-710 Ma and the other
228 at 550-610 Ma, with perhaps a third minor around ca. 450 Ma (Table S3; Fig. 5b). The oldest peak is
229 defined by 13 data (9 cores and 4 rims, Table S3) characterized by Th contents ranging from 13 to 254
230 ppm, with Th/U from 0.11 to 1.77 (most >0.3), these values are typical of magmatic zircon (Tiepel et
231 al., 2004; Linnemann et al., 2011) (Table S3). The dates range from 637 ± 19 Ma to 709 ± 20 Ma with

232 a weighted average of single-analysis concordia ages of 671 ± 15 (MSWD = 6.3; n = 13). The next peak
233 is also composed of 13 data (9 rims and 4 cores, S3) that have Th concentrations between 19-347 ppm
234 with the Th/U ratios ranging from 0.14-1.22 except for three rims (Th/U = 0.02-0.04) (Table S3). These
235 dates are between 550 ± 16 Ma and 608 ± 18 Ma with a weighted average of single-analysis concordia
236 ages of 578 ± 13 Ma (MSWD = 6.1; n = 13) (Fig. 5b).

237 The youngest cluster (group2) is defined by 8 rim data including 5 concordant ones showing Th contents
238 between 3 and 17 ppm (except for one at 196 ppm) and low Th/U ratios of 0.01-0.08 (except for one at
239 0.38) (Table S3; Fig. 5b). Among the five concordant dates, three (Zr27b, Zr43b, Zr41b) yield a
240 concordia age of 339.5 ± 13 Ma (MSWD_(C+E) = 2.8) and the two youngest data (Zr57b, Zr44b) give a
241 concordia age of 305.8 ± 6.8 Ma (MSWD_(C+E) = 0.23). This date is consistent with the lower intercept
242 date obtained by the linear regression on the 4 youngest data (2 concordant and 2 discordant data (Zr20b,
243 Zr42b)) of 305.1 ± 7.8 Ma (MSWD = 0.16). Other data (dotted ellipses) are not taken into account
244 because they are discordant probably due to radiogenic lead loss and common Pb contamination (Fig.
245 5b).

246 *The migmatitic paragneiss from the Agly dam (Ag3B)*

247 Ag3B is a migmatitic paragneiss sampled near the Agly dam composed of Kfs + Qtz leucosomes and
248 Bt + Sill melanosomes, both containing garnet (Fig. 6a). It is located in the upper structural levels of
249 the infrastructure, close to the southern boundary of the D3 corridor (Fig. 3). Small C2 shear zones are
250 located in the melanosomes whereas the leucosomes are weakly deformed. Garnets are elongated and
251 fractured parallel to the S2 foliation. Thus, we suggest that melting and subsequent leucosome
252 crystallization occurred earlier than the C2 event.

253 Monazite crystals from this sample (Ag3B) have been analysed in a thin section in order to preserve
254 textural relationships. Monazite occurs both in the Qtz-Kfs matrix (e.g. Mn7; Mn19, Fig. 6b), as
255 inclusions in the elongated and fractured garnet (e.g. Mn5; Mn10, Fig. 6c and d) and in Bt-Sill shear
256 band (e.g. Mn9; Mn16, Fig. 6e and f). In relation to their textural position, thirty-seven analyses on
257 thirty monazite grains have been performed (Table S2). High to very high Pb, Th and U contents of

258 matrix-monazite or inclusion-monazite inclusion are similar with very wide ranges between 1084-3782
259 ppm (most 1084-2879 ppm), 35693-118463 ppm (most 35693–80990 ppm) and 1587–13134 ppm,
260 respectively. The Th/U ratios are between 3.8 and 29.9. The highest ratios are found in some monazite
261 grains included in the garnet (Table S2).

262 The three matrix-monazite grains analysed (Mn 7, 18 and 19) are anhedral small grains (30 to 60 μm)
263 without clear zonation (Fig. 6b). These analyses yield a concordia age of 292 ± 4 Ma ($\text{MSWD}_{(\text{C+E})} =$
264 1.8; $n = 3$; Fig. 7a).

265 Ten monazite inclusions within garnet (Mn 10, 41, 39, 28, 5, 27, 2, 1, 24 and 26) are anhedral and 50-
266 150 μm in size with sometimes slight patchy zoning in BSE (Fig. 6c and d). They are present in garnet
267 from core to rim and thus grew before or synchronously with garnet crystallization. However, the well-
268 known armouring effect of garnet (e.g. Goncalves et al., 2004; Dumond et al., 2015) is limited by the
269 presence of numerous fractures that may have favoured fluid-assisted dissolution-precipitation of
270 monazite after garnet crystallization. The thirteen analyses yield an upper intercept date of 295 ± 8 Ma
271 ($\text{MSWD} = 1.3$; $n = 13$; Fig. 7b). Among these data, nine yield a concordia age of 290.6 ± 3.4 Ma
272 ($\text{MSWD}_{(\text{C+E})} = 1.3$; $n = 9$). Both dates are similar; the best date estimate probably is the concordia age.

273 Among the sixteen-monazite crystals analysed in the deformed zone, nine are included in sillimanite
274 aggregates and are anhedral, elongated and marking the foliation with patchy zonings (Fig. 6f). Two
275 crystals (Mn 3 and 8) are included in biotite and show sub-euhedral shapes. Five monazite grains (Mn
276 9, 15, 32, 34 and 35) are in contact with both biotite and sillimanite. They are anhedral, stubbier with
277 irregular borders and do not show a preferential orientation (Fig. 6e; Table S2). The spot analyses
278 carried on the monazite crystals included in sillimanite and in biotite yield two similar concordia ages
279 within error of 289 ± 2 Ma ($\text{MSWD}_{(\text{C+E})} = 1.17$; $n = 13$) and 297 ± 9 Ma ($\text{MSWD}_{(\text{C+E})} = 2.6$; $n = 3$),
280 respectively (Fig. 7c). Combining all the analyses (except two) performed on the sixteen-monazite
281 grains in the deformed zone yields a concordia age of 289.7 ± 2.0 Ma ($\text{MSWD}_{(\text{C+E})} = 1.5$; $n = 14$).

282 No correlation is observed within error between the textural position of the various populations (e.g.
283 inclusion vs. matrix), U-Th-Pb contents and dates. Moreover, whatever the textural position of

284 monazite, all dates are similar within uncertainties. Therefore, crystallization of monazite is unrelated
285 to structural location and a single age can be calculated for the whole population. Thirty-one analyses
286 on thirty monazite grains (inclusion and matrix) form a cluster, which yields a concordia age of 290.2
287 ± 1.6 Ma ($MSWD_{(C+E)} = 1.5$; $n = 31$) (Fig. 7d).

288 **Samples from the C2 Shear Zones**

289 The Caladroy Shear Zone (CSZ) is the main C2 high strain zone that separates the supra and
290 infrastructure (Fig. 8), and largely accommodated late-D2 thinning (Bouhallier, 1991; Vanardois et al.,
291 2020; Siron et al., 2020). It appears as a kilometer-thick anastomosed network of mylonitic shear zones
292 (C2) separating lens-shaped lower D2 strain domains where S2 predominates (Fig. 8a, Vanardois et al.,
293 2020). Two meters-thick pegmatitic dykes were sampled in the core of the CSZ, located in the Brosse
294 ravine (Fig. 8b). The pegmatite sample Ag03 is weakly deformed and lies within a low D2 strain
295 domain, whereas sample Ag38 is strongly deformed and located in the core of a C2 shear zone.

296 *The Brosse ravine weakly deformed pegmatite (Ag03)*

297 Sample Ag03 corresponds to a meter-thick dyke that is subconcordant to the S2 foliation within the
298 sillimanite-bearing micaschists (Fig. 8c). The pegmatite contains xenoliths of the surrounding
299 micaschists. The pegmatite consists of a coarse-grained Qtz + Kfs + Pl + Ms + Bt + Tur pegmatitic
300 assemblage, with no clear preferential orientation of minerals, but with a weak solid-state deformation,
301 attested by the recrystallization of quartz grains. Biotite is not chloritized and feldspar is slightly
302 sericitized, indicating limited fluid-rock interaction.

303 Monazite crystals are anhedral, sometimes rounded or in a fragmented form, green and transparent to
304 slightly opaque. BSE imaging shows some grains to have a weakly patching zonation (Fig. S1). Twenty-
305 six analyses on twenty-three crystals were analysed (Table S2). These data show wide ranges with high
306 to very high Pb (5443-13712 ppm), Th (46617-269584 ppm) and U (29933-105937 ppm) contents and
307 moderate Th/U ratios (0.58-9.01; most 0.58-4.13). In the concordia diagram, all these data are
308 concordant between 310 and 270 Ma (Fig. 9a). Two data are younger (dotted ellipses) than the rest,

309 presumably because of minor radiogenic Pb loss. Omitting those two data and an older one yields a
310 concordia age of 290.6 ± 1.6 Ma ($MSWD_{(C+E)} = 1.5$; $n = 23$; Fig. 9a).

311 Zircon is euhedral, prismatic with a shape ratio up to 3:1 and usually metamict and brownish except
312 two crystals, which are transparent and colourless. CL imaging shows that the two colourless zircons
313 have concentric zoning, but for others no zonation could be observed due to the metamictization (Fig.
314 S2). Twenty-five analyses were carried out on twenty zircons of which nineteen yield a lower intercept
315 date of 305.2 ± 2.1 Ma ($MSWD = 0.38$) and among these data, eleven give a concordia age of $304.4 \pm$
316 2.6 Ma ($MSWD_{(C+E)} = 1.03$) (Table S3; Fig. 9b). Except for datum Z9c, the concordant data are
317 characterized by high Pb (102-330 ppm) and U (2425-7356 ppm, most 2425-3568 ppm) contents and
318 low Th (4-13 ppm) concentrations (Table S3). The four discordant data slightly above the concordia
319 curve have a similar range in Pb (113-174 ppm) and U (2532-3838 ppm) contents and higher Th
320 contents (10-132 ppm) than those from the concordant data. All these data have very low Th/U (0.001-
321 0.019; most of them are between 0.001-0.004). Moreover, the core analyses of Zr2, Zr4 and Zr15 are
322 concordant at 1762 ± 22 Ma, 501 ± 15 Ma and 359 ± 10 Ma, respectively (Table S3; Fig. 9b).

323 *The Brosse ravine mylonitic pegmatite (Ag38)*

324 The mylonitic pegmatite (Ag38) is located in a high-strain D2 along a decametric thick C2 shear zone
325 (Fig. 8b). It shows the same mineralogical assemblage as Ag03 with Qtz + Kfs + Pl + Ms + Tur \pm Grt.
326 Feldspar is slightly sericitized. The pegmatite is strongly deformed and totally transposed along the C2
327 shearing plane. Quartz, feldspar, and tourmaline are strongly elongated and stretched along the N20 L2
328 stretching lineation trend (Fig. 8d).

329 Two types of monazite crystals can be distinguished macroscopically, according to their colour, either
330 green and transparent (Mn 1 to 7) or yellow to greenish and slightly opaque (Mn 8 to 17). In both cases,
331 they are anhedral, and have no zonation in BSE. Moreover, they have similar concentrations ($U = 22009$
332 $- 101992$ ppm (most > 50000 ppm); $Th = 42249 - 92063$ ppm; $U/Th = 0,45 - 2,97$) (Table S2). In the
333 concordia diagram, the two populations of monazite cannot be distinguished (Fig. 9c). Twenty-six
334 analyses on seventeen monazites were performed (S2 and Table S2). Except two data (Mn12 and Mn

335 8-1, dotted ellipses), all ellipses are concordant between 250 and 310 Ma and, excluding 5 analyses
336 (dotted ellipse), yield a concordia age of 291.5 ± 1.6 Ma ($MSWD_{(C+E)} = 0.53$; $n = 19$) (Fig. 9c).

337 Zircon crystals are euhedral, brown, usually metamict. In CL, they are uniform enough without real
338 internal structures (Fig. S2). Twenty-four analyses were performed on twenty-two zircons (Table S3).
339 Except data Z4 and Z34, all data have very low Th/U ratios ($\ll 0.1$, most < 0.001) with low Th contents
340 (< 10 ppm). In the Tera-Wasserburg diagram, except two data (Zr6c and Zr29C around 310 Ma), all
341 ellipses have a concordant to sub concordant position at ca. 300 Ma and are aligned along a common-
342 Pb discordia (Fig. 9d). Amongst these twenty-two data, thirteen give a concordia age of 297.6 ± 2.3 Ma
343 ($MSWD_{(C+E)} = 1.4$; Fig. 9d).

344 *The Planèzes mylonitic pegmatite (Ag47)*

345 Sample Ag47 is a 10-meter thick mylonitized pegmatite in the micaschists of the suprastructure, north
346 of the Planèzes village (Fig. 2). This pegmatite is mineralogically similar to the Brosse Ravine
347 pegmatites and consists of Kfs + Qtz + Pl + Ms + Tur assemblage, with slightly sericitized feldspars.
348 The pegmatite shows a strong D2 mylonitization and is transposed along a C2 shear zone. The C2 high-
349 strain planar fabric and L2 lineation marked by elongated quartz and tourmaline crystals are steepened
350 due to Late-D3 deformation (Fig. 3).

351 Only a few zircons could be analysed that are usually anhedral, metamict and brownish-pink coloured.
352 Most crystals preserve at least some crystal faces, although on some others those faces are almost
353 entirely erased. One crystal (Z1) is subhedral, transparent and colourless. Fifteen analyses on seven
354 zircons were performed (Table S3). In the Tera-Wasserburg diagram, all data are concordant or sub-
355 concordant and form two clusters at ~ 490 -530 Ma (group 1) and ~ 300 -330 Ma (group 2) (Table S3;
356 Fig. 10). The three analyses of group 1 were acquired on a single atypical and colourless crystal (Zr1).
357 The Pb, Th and U contents are between 34-95 ppm, 39-69 ppm and 431-1212 ppm, respectively and
358 with low Th/U ratios < 0.1 (i.e 0.045-0.091). Two analyses (Zr1-1 and Zr1-2) yield a concordia age of
359 527.1 ± 9.4 Ma ($MSWD_{(C+E)} = 1.5$; $n = 2$) and the third datum (Zr1-3) gives a younger date at 490 ± 12
360 Ma. The group 2 data were obtained from 12 analyses on 6 zircon crystals showing a very low Th

361 content (<3 ppm), a high to very high U content (1453-3900 ppm) with a very low Th/U ($\ll 0.01$) (Table
362 S3; Fig. 10). Ten ellipses give a lower intercept date at 299.5 ± 2.6 Ma (MSWD = 0.32) and among
363 these data, nine yield a concordia age of 299.7 ± 2.7 (MSWD_(C+E) = 0.56). Two concordant ellipses
364 (Zr5-2 and Zr7-2) yield an older concordia age of 326.6 ± 6.2 Ma (MSWD_(C+E) = 2.6; n = 2) (Table S3;
365 Fig. 10).

366 **Samples from the Proto-D3 Tournefort area**

367 *The Tournefort pegmatitic dyke (Ag08)*

368 Sample Ag08 is a 30-centimeter thick pegmatitic dyke that intrudes the Tournefort diorite (Fig. 11a and
369 b). It cross-cuts the magmatic S3 foliation of the Tournefort diorite in a place where S3 is NE-SW
370 trending and interpreted by Vanardois et al. (2020) as Proto-D3 planar fabrics (Fig. 11b). The pegmatite
371 consists of a Qtz + Kfs + Pl \pm Ms assemblage and shows brittle structures and localized ductile
372 deformation of quartz (Fig. 11c). The feldspars are unaltered.

373 Monazite is anhedral, rounded with few preserved faces, clear and light-yellow coloured. BSE images
374 show that in some crystals, margins are irregular and there are cavities in rims where monazite might
375 have been partly dissolved out. Moreover, some crystals contain mineral inclusions, are fractured and
376 have a weak intergrowth zoning (Fig. S1). Fifteen analyses were carried out on ten monazite crystals
377 characterized by a wide range of Pb (most 1603-5982 ppm), Th (most 81772-190088 ppm) and U (most
378 2084-15431 ppm) contents and Th/U ratios (most 7.1-26.7) (Table S2; Fig. 12a). Except for three
379 analyses (2 discordant and 1 concordant), all these data yield a concordia age of 296.4 ± 2.4 Ma
380 (MSWD_(C+E) = 1.3; n = 13). The difference in date of ~ 45 Ma between the younger concordant date (Mn
381 13) (not plotted because partially outside the range) at 249 ± 9 Ma and the average date of the cluster
382 may be the result of radiogenic Pb loss (Table S2; Fig. 12a).

383 Two zircon types were found in this sample. The first type consists of euhedral, clear, colourless zircon
384 crystals with CL images showing concentric zoning and few inherited cores. The second type is defined
385 by euhedral, metamict, opaque and red crystals and CL images exhibiting mainly grains with cores

386 containing many inclusions and cavities and which are sometimes enveloped by thin and homogenous
387 rims (Fig. S2). Twenty-seven analyses on both cores and rims of eighteen zircon grains were analysed
388 (Table S3). In the Tera-Wasserburg diagram, three inherited cores are concordant at 621 ± 22 Ma, 432
389 ± 16 Ma and 390 ± 15 Ma (Fig. 12b). They have similar Pb, Th and U concentrations, of about 23-32
390 ppm, 83-112 ppm and 207-538 ppm respectively. Their Th/U ratios are 0.16, 0.22 and 0.54 (Table S3).
391 However, the majority of the data are clustered between ca. 350 Ma and 290 Ma (Fig. 12b). In the
392 single-analysis concordia ages histogram, the data are distributed into 2 main populations at ~ 295 Ma
393 and at 320-330 Ma, with an additional data at 353 ± 13 Ma (Fig. 12b; Table S3). The youngest population
394 at 295 Ma is performed on eleven zircon rims from 6 colourless and 5 metamict zircon grains. The six
395 colourless zircons yield concordant data and are characterized by moderate Pb (59-110 ppm) and Th
396 (85-352 ppm) contents and high to very high U (1350-2455 ppm) and with low Th/U ratios (0.06-0.25;
397 most 0.06-0.12). While the rims of five metamict zircon give four discordant data which are
398 characterized by higher Pb (123-225 ppm) and U (2901-5254 ppm) contents and lower Th
399 concentrations (31-82 ppm) and with Th/U at 0.01-0.02 (Table S3). The linear regression on all these
400 data yields a date of 293.8 ± 3.4 Ma by lower intercept (MSWD = 0.16; n = 11). Among these data,
401 nine give a concordia age of 295.5 ± 3.8 Ma (MSWD_(C+E) = 1.9) (Fig. 12b). The best date estimate is
402 probably the concordia age. The second population at 320-330 Ma consists of twelve concordant data
403 performed on 10 colourless crystals (8 cores and 4 rims). These data have low to moderate in Pb (10-
404 81 ppm) and in Th (36-168 ppm) and moderate to high U (199-1695 ppm most 199-465 ppm) contents
405 and moderate Th/U ratios (0.1-0.42 most 0.14-0.42) (Table S3). The highest U contents (1131 and 1695
406 ppm) associated with the lowest Th/U ratios (0.01) are obtained on the rims of two zircon grains (Z15
407 and Z23). These twelve data yield a concordia age of 323.3 ± 3.8 Ma (MSWD_(C+E) = 0.7; n = 12) (Fig.
408 12b).

409 *The garnet-bearing leucogranite dyke (Ag06)*

410 Sample Ag06 was collected north of the Tournefort diorite and east of the Saint-Arnac granite (Fig.
411 11a). Interference between far field deformation and local deformation induced by pluton emplacement
412 makes a complex strain pattern where D2, Proto-D3 and D4 planar fabrics are observed (Fig. 11a)

413 (Vanardois et al. 2020). The sample Ag06 consists of a 2-meter thick peraluminous leucogranite dyke.
414 This dyke cross-cuts the Tournefort diorite magmatic foliation, the S2 foliation observed in surrounding
415 partially melted micaschists and M2 isograd (Fig. 11a). Field relationships suggest that the
416 emplacement of the leucogranite (Ag06) post-dates M2 metamorphic peak, the emplacement of the
417 Tournefort diorite and the Proto-D3 deformation. This interpretation is consistent with the lack of solid-
418 state deformation of the magmatic assemblages consisting of Kfs + Pl + Qtz + Grt + Ms (Fig. 11c;
419 Vanardois et al. 2020).

420 Most monazite crystals are subhedral but a few grains are slightly rounded and transparent, all are clear
421 to pale yellow. BSE imaging shows that most grains present a weak concentric or intergrowth zoning
422 (Fig. S1). Twenty-six analyses on twenty monazite grains were performed (Table S2; Fig. 12c). They
423 are characterized by high Pb (1578-4029 ppm) and U (506-9127 ppm) and very high Th (37498- 140262
424 ppm) concentrations giving a range of relatively high to very high Th/U ratios (6.2-138; most 26.2-138)
425 (Table S2). Except for two analyses (Mn7, Mn19r, dotted ellipses)), all data are concordant to
426 subconcordant around 290-310 Ma (Fig. 12c). Twenty-two data give a concordia age of 298.2 ± 2.7 Ma
427 ($MSWD_{(C+E)} = 1.7$; $n = 22$) (Fig. 12c).

428 Zircon crystals are relatively small ($\sim 100 \mu\text{m}$), transparent, slightly pink to opaque pink-brown and
429 mostly are euhedral prismatic crystal fragments. CL imaging shows strong evidence of concentric or
430 oscillatory igneous growth zoning with no obvious cores (Fig. S2). Twenty-eight analyses were carried
431 out on twenty-one zircon grains (Fig. S2; Table S3). These data are characterized by a wide range of
432 Pb (37-195 ppm), Th (94-1134 ppm) and U (807-4076 ppm) concentrations and Th/U ratios (0.08-0.67,
433 most 0.11-0.67) (Table S3). The distribution of all ellipses near 300 Ma in the Tera-Wasserburg diagram
434 suggests that discordant analyses are probably affected by a common Pb contamination (Fig. 12d). The
435 linear regression on the data set gives a date of 295.0 ± 2.9 Ma by lower intercept ($MSWD = 0.10$; $n =$
436 28) and the eleven data yield a concordia age of 298.3 ± 3.2 Ma ($MSWD_{(C+E)} = 1.4$; $n = 11$) (Fig. 12d).
437 Both dates are equal within the uncertainties and the best date estimation is the concordia age.

438 **Samples from the Late-D3 Tournefort Deformation Zone**

439 *The Vivier orthogneiss (Ag48)*

440 The Vivier orthogneiss (Ag48) is a 200-meter-thick laccolith containing paragneiss and marble
441 elongated xenoliths. It is located inside the D3 corridor at its westernmost edge (Fig. 3). It is composed
442 of a Qtz + Kfs + Grt + Bt ± Pl assemblage. It is partially molten and deformed at high temperatures
443 with myrmekites having replaced the margins of Kfs, and recrystallization of quartz and feldspars. The
444 main fabric observed, which is vertical, is interpreted as a late-D3 foliation. The partial melting affecting
445 the Vivier orthogneiss sample (Ag48) is pre-D3.

446 Monazite crystals are subhedral to anhedral, light yellow and transparent. BSE images show that most
447 crystals present a patchy zoning occasionally surrounded by a rim (Fig. S1). The analysed crystals have
448 Pb (2076-5805 ppm), Th (63234-195033 ppm) and U (3391-8618 ppm) contents and Th/U ratios (9.18-
449 31.17), which vary from crystal to crystal and within the same monazite (Table S2). Twenty-eight spot
450 analyses on eighteen monazite crystals were performed (Table S2; Fig. 13a). In the concordia diagram,
451 all ellipses yield a concordia age of 299.7 ± 1.7 Ma ($MSWD_{(C+E)} = 1.4$; $n = 28$) without apparent
452 difference between the rims and cores of the various crystals.

453 Zircon crystals are euhedral, transparent and colourless to slightly pinkish. CL images also show
454 complex internal textures such as the presence of inherited cores and concentric oscillatory zoning and
455 patchy zoning textures (Fig. S2). Thirty-six analyses were carried out on twenty zircon grains (Table
456 S3; Fig. 13b). Among these data, thirty-three are concordant between ca. 630 Ma and 290 Ma. In the
457 single-analysis concordia ages histogram, the data are distributed into 4 variable-sized populations: two
458 minor ones at 430-490 Ma (group 1) and 570-630 Ma (group 2) and two major groups at 510-570 Ma
459 (group 3) and 300-350 Ma (group 4) and (Fig. 13b).

460 Group 1 dates are determined from 4 rims and 1 core that have moderate Pb (23-103 ppm) and Th (21-
461 58 ppm) contents and low Th/U ratios (0.03-0.18). These five data are ranging from 446 ± 12 Ma to
462 479 ± 12 Ma and yield a weighted average of 462 ± 17 Ma ($MSWD = 5.2$) (Fig. 13b; Table S3).

463 Group 2 dates are acquired on four zircon cores, which are characterized by moderate Pb contents (11-
464 74 ppm) and variable Th (26-300 ppm) and U (113-713 ppm) concentrations, with Th/U ratios ranging
465 from 0.08-0.42. They yield a concordia age of 597.2 ± 7.7 Ma ($MSWD_{(C+E)} = 0.68$) (Fig. 13b; Table
466 S3).

467 Group 3 dates are obtained from 10 cores and 3 rims. Pb and Th contents ranging from 11-158 ppm and
468 20-148 ppm, respectively, characterize these data. The U contents of the rims (758-2088 ppm) are
469 higher than those of the cores (131-645 ppm). Th/U ratios of the cores (0.06-0.6; most 0.06-0.25) are
470 thus higher than those of the rims (0.05-0.03). These data give a weighted average of 541 ± 11 Ma
471 ($MSWD = 6.6$; $n = 13$). Among these 13 dates, nine yield a concordia age of 551.8 ± 4.8 Ma
472 ($MSWD_{(C+E)} = 1.1$; $n = 9$) (Fig. 13b, Table S3).

473 Group 4 dates were determined from rims of ten zircon crystals characterized by moderate Th and Pb
474 contents ranging from 5 to 18 ppm and 20 to 31 ppm, respectively, and by very low Th/U ratios from
475 0.01 to 0.03 (Table S3). Seven of these zircon rims yield a concordia age of 303.9 ± 5.5 Ma ($MSWD_{(C+E)}$
476 $= 2.5$). The rims of three zircon grains Zr31, Zr18 and Zr27 have older dates at 344 ± 9 Ma, 323 ± 9 Ma
477 and 391 ± 11 Ma, respectively. These dates are probably meaningless because they correspond to a
478 mixture between an old core (~ 550 Ma) and a younger rim (probably ~ 300 Ma) (Fig. 13b, Table S3).

479 *Latour de France leucogranite (Ag51)*

480 The Latour-de-France leucogranite (Ag51) is located to the southwest of Latour de France village, in
481 the infrastructure (Fig. 2 and 3). It is a 50-meter thick pluton composed of Qtz + Kfs + Pl + Bt + Grt +
482 Ms. It shows no visible solid-state deformation but microstructures such as myrmekites replacing Kfs
483 margins, plastic deformation of quartz indicated by chessboard extinction and microfractures in Kfs
484 infilled by quartz indicate that the leucogranite was deformed under sub-magmatic conditions (Fig.
485 14a). The pluton cross-cuts S2 foliations and C2 shear zones and was emplaced in a kilometre-scale D3
486 fold hinge (Fig. 3; Vanardois et al. 2020). These observations suggest that the Latour de France
487 leucogranite sample (Ag51) is syn-late-D3.

488 Monazite is sub-euhedral prismatic with a shape ratio up to 2:1, transparent and light-yellow coloured.
489 BSE images of most crystals show that the centre with a patchy zoning while rims are characterized by
490 a darker, slight concentric zoning (Fig. S1). The analysed spots have high Pb (2611-4672 ppm), high to
491 very high U (5958 – 14794 ppm) and very high Th (75731 – 147318 ppm) concentrations with a range
492 of relatively moderate Th/U (6.3 - 16.6) (Table S2). Twelve analyses were performed on 10 crystals
493 (Fig. 14b; Table S2). These twelve data yield a concordia age of 291.0 ± 2.0 Ma ($MSWD_{(C+E)} = 0.27$; n
494 = 12) (Fig. 14b).

495 Most of the zircon crystals analysed are euhedral, either prismatic with a shape ratio up to 3:1 or stubbier
496 with a shape ratio of 1:1. They are transparent, slightly pink to opaque pink-brown. CL imaging shows
497 strong evidence of concentric or oscillatory igneous growth zoning and the presence of some inherited
498 cores (Fig. S2). Twenty-two analyses were carried out on nineteen zircon grains (Fig. 14c; Table S3).
499 Among these analyses, eighteen have a concordant to discordant position around 290 Ma suggesting a
500 common Pb contamination. The linear regression calculated with these 18 data yields a date of $288.4 \pm$
501 3.3 Ma by lower intercept ($MSWD = 0.36$; $n = 18$) and amongst nine data give a similar concordia age
502 of 289.4 ± 4.2 Ma ($MSWD_{(C+E)} = 1.6$; $n = 9$) (Fig. 14c). These data are obtained on rims and cores of
503 crystal and present Th/U ratios ranging between 0.004 and 0.26 (most are between 0.004-0.06) (Table
504 S3). Moreover, the analyses of two zircon cores (Zr12c, Zr24c) yield a concordia age of 549 ± 11 Ma
505 ($MSWD_{(C+E)} = 1.7$). Furthermore, a third analytical point (Zr36c) is concordant at 684 ± 23 Ma (Table
506 S3; Fig. 14c). The Th/U ratios of these three data are between 0.43 and 0.17.

507 **Interpretation and discussion**

508 **Pre-Variscan history: Cadomian and Ordovician magmatism**

509 Two samples collected in the infrastructure, near Le Vivier (Ag48, Ag57), show an early and complex
510 history with inherited Precambrian and Ordovician zircon population ages (Table 1; Fig. 5b and 13b).
511 The single-analysis concordia ages histograms of the Vivier deformed leucogranite (Ag57) and the
512 Vivier orthogneiss (Ag48) highlight the presence of two major date populations at 630-710 Ma and at
513 550-610 Ma and three variable-sized populations with a main one at 510-570 Ma and two minor ones

514 at 430-490 Ma and 570-630 Ma (Fig. 12b) respectively. These Neoproterozoic and Cambrian zircon
515 populations could be correlated with zircon crystallization events related to the development of the Pan-
516 African (750-600 Ma) and Cadomian (590-540 Ma) orogens (Linnemann et al. 2014) (Fig. 5b).
517 Moreover, the presence of the Ordovician zircon population in the Ag48 sample, that are essentially
518 zircon rims, is also an evidence for an Ordovician tectono-thermal event, which is possibly related to
519 the emplacement of the magmatic protolith of the Rivérole orthogneiss at 461 ± 3 Ma in the
520 infrastructure of the Agly massif (Paquette et al. 2021). The concordia age obtained on the Vivier
521 orthogneiss (Ag48) at 551.8 ± 4.8 Ma is interpreted as the magmatic protolith emplacement age, and
522 indeed, it is consistent with the ages at ca. 540-530 Ma obtained on five igneous rocks from the Agly
523 massif infrastructure by Tournaire Guille et al. (2019). Similar Ordovician and Cambrian magmatism
524 is widely documented in the Pyrenees (Deloule et al. 2002; Castinieras et al. 2008; Casas et al. 2010,
525 2015; Liesa et al. 2011; Martinez et al. 2011; Lemirre 2016; Marti et al., 2019) and in the French Central
526 massif (Pin and Lancelot 1982; Roger et al. 2004; Alexandre 2007; Lotout et al. 2017) and inherited
527 Pan-African and Cadomian zircons are also common in the various massifs from the southwestern
528 segment of the Variscan belt (e.g. Melleton et al. 2010; Denèle et al., 2014; Schnapperelle et al. 2020;
529 Margalef et al., 2016; Roger et al. 2015, 2020). Their occurrence are related to a possible source region
530 of the northeastern Gondwana margin (von Raumer et al. 2015; Linnemann et al. 2014; Couzinié et al.
531 2014; Chelle-Michou et al. 2017; Stephan et al. 2019).

532 **Middle Carboniferous crustal partial melting and magmatism event (ca. 340-320 Ma)**

533 Three zircon rims from the Vivier leucogranite (Ag57) and two inherited cores of slightly metamict
534 zircon from the Planèzes mylonitic pegmatite (Ag47) yielded concordia ages of 339.5 ± 13 Ma and of
535 326.6 ± 6.2 Ma, respectively (Fig. 5b, 10b). The Tournefort undeformed pegmatite (Ag08) has a zircon
536 population (cores and rims) that yielded a concordia age of 323.3 ± 3.8 Ma (Fig. 12b). These three dates
537 are similar within error and define a 340-320 Ma event. Similarly, monazite and zircon ages of 340-320
538 Ma have been reported in migmatites from the southern French Central Massif (Faure et al. 2014), in
539 migmatites and granites of the PAZ (Mezger and Gerdes 2016; Lopez-Sanchez et al., 2019;
540 Schnapperelle et al. 2020) and migmatites of the NPZ (Lemirre 2016). However, the origin of this

541 Visean/Serpukhovian magmatic and metamorphic event in the foreland is still debated (Roger et al.
542 2015; Schnapperelle et al. 2020; Cugerone et al. 2021). Thermobarometric estimates on the Montagne
543 Noire (MN) gneiss dome suggest that, between 330 and 320 Ma, the continental crust was slightly
544 overthickened with a partially molten lower-middle crust, at a depth between 30 and 40 km (Trap et al.
545 2017; Whitney et al. 2020). In the Agly massif, this early event is only identified through inherited
546 zircon populations. Although we are not able to constrain the relationships between this early thermal
547 event and the strain fabrics, we propose that the ~340-320 Ma record could be attributed to the D1 or
548 early-D2 deformations.

549 **Peak of magmatism at ca. 305 Ma**

550 Our results, as well as additional data from the literature, show that most of the Agly massif magmatic
551 bodies range in crystallization age between 308 and 304 Ma (Olivier et al. 2004, 2008; Tournaire Guille
552 et al. 2019) (Fig. 15). The zircon grains from the two Brosse Ravine pegmatites (Ag38, Ag03) show
553 high U and Th contents and very low Th/U ratios (most <0.004) (Table S3). Although the low Th/U
554 ratios (<<0.01) is commonly interpreted as the fingerprint of metamorphic crystallization, magmatic
555 zircons with low Th/U ratios (<0.1) have also been reported in high-SiO₂ and/or peraluminous
556 granitoids (Lopez-Sanchez et al., 2016). Thus, we interpret the zircon concordia age at 304.4 ± 2.6 Ma
557 from the weakly deformed Ag03 pegmatite (Fig. 9b) as the emplacement age. A similar zircon
558 concordia age at 305.8 ± 6.8 Ma (Fig. 5b) is given by the undeformed Vivier leucogranite (Ag57),
559 emplaced as a sill into the flat-lying S2 foliation. The sills of Ansignan charnockite and Cassagnes
560 granite have been dated to 307 ± 3 Ma and to 308 ± 3 Ma (Tournaire Guille et al. 2019). They are
561 intrusive into the migmatitic S2 foliation with concordant to slightly discordant cross-cutting
562 relationships (Vanardois et al., 2020). This argues for the development of suprasolidus S2 foliation
563 before 308 Ma. Several ID-TIMS analyses and one LA-ICPMS analysis on syn-S2 charnockitic sills
564 yield emplacement ages at ca. 315 Ma (Fig. 15; Postaire 1982; Respaut and Lancelot 1983; Olivier et
565 al. 2004; Tournaire Guille et al. 2019) that might bracket the oldest development of D2 deformation.
566 The undeformed Vivier leucogranite (Ag57) also intrudes into the S2 and gives a zircon concordia age
567 at 305.8 ± 6.8 Ma and a monazite concordia age at 299.7 ± 1.7 Ma (Fig. 5a). Both zircon and monazite

568 dates are similar within uncertainties but it is more likely that the emplacement of the Vivier
569 leucogranite is best constrained by the zircon concordia age at 305.8 ± 6.8 Ma. The 299.7 ± 1.7 Ma
570 monazite age might represent a partial reset during late D2 fluid-rock interactions. Indeed, experimental,
571 petrological and field studies (Roger et al. 2020 and references therein) have shown that fluid-assisted
572 dissolution-precipitation mechanisms are effective in altering the chemical and isotopic composition of
573 monazite, even at low temperatures (Hawkins and Bowring 1997; Townsend et al. 2000). These results
574 are consistent with Siron et al. (2020) that dated M2 partial melting and S2 planar fabric at ca. 305 Ma
575 within kinzigites from different structural levels of the infrastructure.

576 The U-Th-Pb ages of the syn-D3 Tournefort diorite and Saint-Arnac granite in the Tournefort
577 Deformation zone (TDZ) between 308 and 304 Ma (Olivier et al. 2004, 2008) also constrain the timing
578 of the Proto-D3 dextral strike-slip shearing (Fig. 15). We propose that the D3 deformation started with
579 the development of a vertical S3 within the dextral Proto-D3 shear zone at ca. 308 Ma. Vertical planar
580 fabrics are pathways for the ascent of melts from the lower crust towards the middle and upper crusts
581 (e.g. de Saint-Blanquat et al. 1998; Handy et al. 2001). The southern part of the St-Arnac pluton and
582 Tournefort diorite bear magmatic foliations parallel with the D3 foliation and the vertical migmatitic
583 lineation suggests a vertical ascent of the magmas (Olivier et al. 2008; Vanardois et al. 2020). The
584 northern part of the St-Arnac pluton is structured by gently dipping magmatic foliations and N050-
585 trending lineation indicating a NE directed horizontal expansion that is consistent with the D3 dextral
586 bulk kinematics during syn-tectonic pluton emplacement (Olivier et al. 2008).

587 **Late Carboniferous-early Permian metamorphism and deformation (ca. 300-295 Ma)**

588 Our U-Th-Pb result reports an age group between ca. 300 and 295 Ma. The age of 297.6 ± 2.3 Ma
589 obtained on zircon of the mylonitic pegmatite (Ag38) is interpreted as the synkinematic emplacement
590 of the pegmatite during D2 strain localization along C2 shear zones (Fig. 9d). Zircon rims and cores
591 from the syn-C2 Planèzes mylonitic pegmatite (Ag47) located in the micaschists of the suprastructure
592 yield a concordia age at 299.7 ± 2.7 Ma (Fig. 3 and 9). This date is consistent with the emplacement
593 age of the Brosse Ravine pegmatite (Ag38) and can be interpreted as the syn-C2 emplacement age of

594 the Planèzes pegmatite. Tournaire Guille et al. (2019) dated partial melting of a paragneiss at 299 ± 4
595 Ma and the crystallization of leucogranites in the infrastructure at 307 ± 3 and 298 ± 3 Ma (Fig. 15).
596 The range of ages around 300 Ma are very consistent with the ages of ~ 296 to 300 Ma ages recently
597 obtained on monazite overgrowths from mylonitized kinzigites (Siron et al. 2020) and might constrain
598 the sub-solidus, solid-state, deformation during the onset of the cooling evolution of the Agly massif.

599 The undeformed garnet-bearing leucogranite dyke (Ag06) that crosscuts both the magmatic Proto-D3
600 foliation and the S2 foliation (Fig. 11a) yields zircon and monazite concordia ages at 298.3 ± 3.2 and
601 298.2 ± 2.7 Ma (Fig. 12c and d). Zircon rims and monazites from the undeformed Tournefort pegmatitic
602 dyke (Ag08) yield similar concordia ages at 295.5 ± 3.8 Ma and 296.4 ± 2.4 Ma (Fig. 12a-b). These
603 dates record the emplacement ages of the Ag06 and Ag08 dyke intrusions that crosscut the Proto-D3
604 foliation at ca 300-295 Ma. Finally, the Vivier orthogneiss sample (Ag48) is D3 deformed and yields
605 concordia age on zircon and monazite at 303.9 ± 5.5 Ma and 299.7 ± 1.7 Ma, respectively (Table 1, Fig.
606 13). Both dates are similar within error bars. We interpret the monazite concordia age at ca. 300 Ma as
607 the best age estimate of peak D3 deformation.

608 **Last-stage event at ca. 290 Ma**

609 Monazite from the Ag03 and Ag38 pegmatites gives concordia ages at 290.6 ± 1.6 Ma and 291.5 ± 1.6
610 Ma, respectively (Fig. 9a and b). Both pegmatites are located along a D2 high-strain zone (i.e. Caladroy
611 Shear Zone) (Fig. 3a). There is no evidence of garnet- or biotite-breakdown reactions in these samples
612 that could have induced monazite crystallization. Thus, we interpret these dates as the age the final stage
613 of C2 strain localization in the Caladroy shear zone. It may correspond to the timing of deformation-
614 recrystallization leading to a reset of the U-Th-Pb isotopic system via fluid-assisted, syn-kinematic,
615 dissolution/precipitation monazite processes. The migmatitic paragneiss (Ag3B), from the upper
616 structural levels of the infrastructure, shows a well-developed syn-partial melting S2 foliation that is
617 also affected by localized millimeter-thick C2 shear zones. Irrespective of their textural position (e.g.
618 included in garnet or in C2 high strain zones), all monazite dates give a concordia age at 290.2 ± 1.6
619 Ma (Fig. 7d). The lack of preservation of older ages in monazite included in peritectic phases like garnet,

620 the numerous fractures in garnet, and the absence of garnet-consumption (Fig. 6) suggest that monazite
621 were reset or re-crystallized during a penetrative fluid-rock interaction during the C2 shearing. In
622 comparison with aforementioned ages, the C2 subsolidus shearing started at ca. 300 Ma and lasted until
623 at least 290 Ma.

624 The event at 290 Ma is also recorded in Late-D3 structures. The Latour-de-France leucogranite (Ag51)
625 emplaced in a F3 fold hinge along the southern edge of the D3 corridor (Fig. 3c). It has been dated by
626 similar concordia ages obtained on zircon and monazite at 289.4 ± 4.2 Ma and 291 ± 2 Ma, respectively
627 (Fig. 14). This date at ca. 290-291 Ma is interpreted as the emplacement age of the Latour-de-France
628 leucogranite in the upper part of the infrastructure, contemporaneously with D3 folding (Fig. 3c).
629 Crystallization of these magmatic bodies may have provided hydromagmatic fluids that could be partly
630 responsible for the reset of monazite at ca. 290 Ma. In the Cap de Creus (PAZ), Van Lichterveld et al.
631 (2017) documented a late post-solidus, hydrothermal remobilization at 290 Ma and coeval magmatism
632 in a wrench tectonic regime (Carreras and Druguet 2014).

633 **Tectonic implications**

634 In the PAZ, flat-lying foliations with top-to-the-south kinematics have been described and interpreted
635 as evidence of an early nappe stacking event (Denèle et al. 2009, 2014). These foliations were mostly
636 transposed by pervasive dextral transpression (Gleizes et al. 1998a; Carreras and Druguet 2014)
637 associated with a longitudinal extrusional crustal flow (Cochelin et al. 2017, 2021). A similar evolution
638 is described in the Montagne Noire where a nappe stacking event (Charles et al. 2009; Faure et al. 2014)
639 was followed by a pervasive dextral wrenching in a transtensional regime inducing a longitudinal flow
640 of the partially molten crust between 315 and 300 Ma (Rabin et al. 2015; Roger et al. 2015; Trap et al.
641 2017). Some authors recently proposed that, prior to the longitudinal flow, a gravity-driven flow of the
642 partially molten crust from the northward orogenic plateau towards its southern foreland occurred at ca.
643 320 Ma (Whitney et al. 2015; Roger et al. 2020; Vanderhaeghe et al. 2020). However, the pervasive
644 deformation induced by the dextral wrenching in the PAZ and in the Montagne Noire prevents the full
645 investigation of this hypothesis.

646 On the other hand, the Agly massif is fortunately only affected by local transcurrent tectonics, which
647 allows to discuss the origin of the flat-lying foliation. Initially, this sub-horizontal foliation (S2) in the
648 Agly massif was also interpreted as a southward nappe-stacking event (Bouhallier et al. 1991; Olivier
649 et al. 2004). Nevertheless, Vanardois et al. (2020) recently emphasized the existence of a suprasolidus
650 early planar fabric (S1) probably representing relics of crustal thickening, as well as the flat-lying S2
651 foliation coeval with the crustal thinning of the massif documented by Siron et al. (2020). Olivier et al.
652 (2004) highlighted top-to-the-South kinematics of the supra-solidus S2 foliations whereas the CSZ
653 located at the anatectic front displays top-to-the-North kinematics (Bouhallier et al. 1991; Vanardois et
654 al. 2020). In addition, Siron et al. (2020) documented a crustal thinning of ca. 5 km induced by the CSZ.
655 Considering the low dip of the CSZ (ca. 10-20° northward), such crustal thinning necessitated a
656 horizontal displacement of at least 15-30 km between the infra- and suprastructure. Therefore, we
657 propose that the supra-solidus S2 foliation developed in response to a horizontal flow of the partially
658 molten crust towards the South (Fig. 16a). Our U-Th-Pb results and compilation on the Agly massif
659 highlight that the S2 foliation developed at least at ca. 315 Ma and very likely at ca. 325-320 Ma during
660 the onset of partial melting (Fig. 15). HT metamorphism and migmatization between ca. 340–320 Ma
661 has been already documented in the NPZ and PAZ (Lemirre 2016; Mezger and Gerdes 2016; Lopez-
662 Sanchez et al., 2019; Schnapperelle et al. 2020), which might indicate that the whole Variscan Pyrenees
663 have also been affected by this southward horizontal flow. In the French Massif Central, the high-
664 temperature/medium-pressure metamorphism and the emplacement of syntectonic plutons from 345 to
665 310 Ma is interpreted as the record of a major Carboniferous thermal anomaly that was responsible for
666 the building of the orogenic plateau by gravity-driven lateral flow of the partially molten orogenic root
667 toward the south (Whitney et al. 2015; Vanderhaeghe et al. 2020; Pitra et al. 2021). A similar process
668 of gravity-driven flow has also been proposed in other Variscan massifs (Schulmann et al. 2008, 2014;
669 Diez Fernandez and Pereira 2016; Pereira et al. 2018). A channel flow progressing from the French
670 Central Massif to the Pyrenees would necessitate synchronous extension setting in the hinterlands and
671 compressional regime in the forelands (Rey et al., 2010; Whitney et al. 2013), but our results rather
672 suggest coeval extension in both hinterlands and forelands between 325-310 Ma. Considering the
673 presence of a Viséan – Serpukhovian magmatism and metamorphism in the PAZ and NPZ (Mezger and

674 Gerdes 2016; Schnapperelle et al. 2020; Cugerone et al. 2021; this study), it seems likely that the lower
675 crust of the Variscan Pyrenees was already in high-temperature conditions at 325-310 Ma and probably
676 molten. Therefore, we propose that the whole lower crust of the PAZ, NPZ and Montagne Noire melted
677 at ca. 325-310 Ma and flowed towards the South over short to moderate distances (Fig. 17a), rather than
678 being implicated in a large-scale horizontal channel flow from the northern French Central Massif to
679 the Pyrenees..

680 The syn-tectonic emplacements of the Tournefort diorite and St-Arnac granite in the TDZ (Vanardois
681 et al. 2020) indicate that the dextral wrenching started at ca. 308 Ma in the Agly massif, acting as
682 pathways for melt, enhancing the emplacement of plutons in the upper crust (Fig. 16b and c). Similar
683 emplacement of plutons driven by vertical dextral shear zones at 310-300 Ma are widely described in
684 the PAZ (e.g. Gleizes et al. 1998b, 2001, 2006; Aujérac et al. 2004; Román-Berdiel et al. 2006; Antolín-
685 Tomás et al. 2009) or in the Montagne Noire (Trap et al. 2017; Roger et al. 2020), synchronously with
686 the longitudinal flow of the lower crust (Cochelin et al. 2017, 2021; Trap et al. 2017; Roger et al. 2020).
687 The limited dextral deformation in the Agly massif and in the other areas of the NPZ compared to the
688 PAZ and the Montagne Noire is interpreted as a strain gradient across a lithospheric-scale ductile dextral
689 wrench zone represented by the PAZ (Fig. 17b). In the PAZ, during ongoing transpression, the high-
690 strain dextral shearing reworked the flat-lying foliations related to gravity-driven flow into a
691 longitudinal flow. On the contrary, in the Agly massif, the dextral wrenching remained limited within
692 the partially molten crust, which was still recording southward flow until ca. 300 Ma (Fig. 16b and c,
693 17b). Rey et al. (2017) have demonstrated that local contractional structures can be produced by flow
694 of the molten crust during extensional regime, which could correspond to the coeval D2 extensive and
695 D3 compressive structures in the Agly massif.

696 These results highlight a high-temperature protracted event responsible for crustal partial melting for at
697 least 15-20 Ma. The origin of the heat supply needed necessary to produce these high-temperature
698 conditions in the southern part of the Variscan belt as well as the source of the mantle-derived magmas
699 remain controversial. Several authors proposed deep thermal anomalies related to the delamination of
700 the lithospheric mantle induced by a slab roll-back in the French Central Massif (e.g. Laurent et al.

701 2017; Vanderhaeghe et al. 2020) or affecting the whole Gondwana lithosphere (Lemirre et al., 2019),
702 to mantellic plumes in the whole Variscan belt (Franke 2014, 2017), to ridge subduction and slab
703 window formation in the massifs of southwestern Iberia (Rodriguez et al. 2022; Pereira et al. 2022) or
704 to a sub-lithospheric or intra-crustal relamination and magmatic flow as recently proposed in the
705 Bohemian massif (Maierova et al. 2018, 2021).

706 After the crystallization of most of the anatectic melts in the infrastructure of the Agly massif, the
707 dextral wrenching lasted until 290 Ma in the TDZ (Fig. 15). Our results also highlight that C2 subsolidus
708 flat-lying shear zones were still active at ca. 290 Ma (Fig. 15) with top-to-the-North kinematics
709 (Vanardois et al. 2020). We propose that these shear zones accommodated local extensional regime in
710 the D3 dextral low-strain domains within the NPZ (e.g. Denèle et al. 2014), while transpression was
711 still active in the PAZ and in the Montagne Noire (Cochelin et al. 2017; Roger et al. 2020) (Fig. 17c).
712 In the PAZ and NPZ, Permian magmatism and volcanism in basins has been emphasized by numerous
713 geochronological studies (Denèle et al. 2012; Rodriguez-Mendez et al., 2014; Druguet et al. 2014;
714 Pereira et al., 2014; Lemirre 2016; Kilzi et al., 2016; Van Lichtervelde et al. 2017; Lopez-Sanchez et
715 al., 2018; Poitrenaud et al. 2020; this study). These Permian volcanic and plutonic rocks highlight that
716 the Pyrenean crust was still in anomalous high thermal conditions at the end of the Variscan orogeny.
717 The origin of these Permian high-thermal conditions may be related to a combination of the Paleotethys
718 subduction and an extensive-transpressive setting (e.g. Debon and Zimmermann, 1993; Lago et al., 2004;
719 Gil-Imaz et al., 2012; Pereira et al., 2014).

720 **Conclusion**

721 Our geochronological results and the compilation of available ages on the Agly massif indicate that the
722 Variscan lower-middle crust was partially molten from ca. 325 to 300 Ma. These new results emphasize
723 the first evidence of middle Carboniferous event at ca. 325 Ma in the Agly massif. We also highlight a
724 partitioning of the deformation between flat-lying foliations D2 and a dextral shear zone D3 from ca.
725 308 Ma to 290 Ma. The compilation of geochronological data on the Agly massif and a comparison
726 with tectonic evolutions known for the Montagne Noire and of the Pyrenean Axial Zone allow us to

727 propose a tectonic evolution for the southern edge of the French Central Massif: (i) the maturation of
728 the orogenic crust induced the widespread partial melting of the lower-middle crust in hinterlands and
729 forelands. This was responsible for a horizontal flow from the French Central Massif to the PAZ towards
730 the South at ca. 325 Ma. (ii) Dextral wrenching affecting the whole Variscan belt became pervasive in
731 the Montagne Noire and in the PAZ and reoriented the southward flow into an E-W longitudinal flow,
732 while the NPZ was only locally affected by this dextral wrenching that did not reorient the southward
733 flow. (iii) The crystallisation of most of the anatectic melts stopped the flow of the lower crust at ca.
734 300 Ma. The dextral wrenching remained active until 290 Ma in the Agly massif, the PAZ and the MN.
735 Synchronously with the local wrenching in the TDZ of the Agly massif, subsolidus C2 shear zones
736 accommodated a local extensional regime in the NPZ until ca. 290 Ma.

737 **Acknowledgments**

738 We dedicate this article to Jean-Louis Paquette who sadly passed away in June. This research was
739 supported by the BRGM through the Référentiel Géologique de la France program (RGF program). We
740 thank Cyprien Astoury for mineral separation. Didier Convert provided generous support with thin
741 section preparation. We thank the MIMENTO technology center for the SEM provision.

742 **Declarations**

743 Conflict of interest: The authors declare that they have no known competing financial interests or
744 personal relationships that could have appeared to influence the work reported in this paper.

745

746 **References**

- 747 Aguilar C, Liesa M, Castiñeiras P, Navidad M (2013) Late Variscan metamorphic and magmatic evolution in the
748 eastern Pyrenees revealed by U–Pb age zircon dating. *J Geol Soc London* 171:181-192.
- 749 Alexandre P (2007) U–Pb zircon SIMS ages from the French Massif Central and implication for the pre-Variscan
750 tectonic evolution in Western Europe. *C R Geosc*, 339:613-621.

751 Althoff F, Barbey P, Pons J (1994) La charnockite d'Ansignan et le granite de Saint-Arnac, témoins d'une
752 extension crustale d'âge hercynien dans le massif de l'Agly (Pyrénées Orientales, France). CR Acad Sci
753 Paris 319:239-246.

754 Andrieux P (1982a) Conditions de cristallisation et évolution paragéométrique d'une charnockite hercynienne: le
755 complexe granulitique d'Ansignan (massif de l'Agly, Pyrénées-Orientales). B Minéral 105:253–266.

756 Andrieux P (1982b) La charnockite d'Ansignan (Massif d'Agly, Pyrénées Orientales). Mise en place et évolution
757 paragéométrique. Introduction à l'étude des équilibres grenat – orthopyroxène. 3rd Cycle Thesis, Clermont-
758 Ferrand (France): Univ. Blaise Pascal.

759 Antolín-Tomás B, Román-Berdiel T, Casas-Sainz A, Gil-Peña I, Oliva B, Soto R (2009) Structural and magnetic
760 fabric study of the Marimanha granite (Axial Zone of the Pyrenees). Int J Earth Sci 98: 427–441.

761 Auréjac JB, Gleizes G, Diot H, Bouchez JL (2004) Le complexe granitique de Quérigut (Pyrénées, France) ré-
762 examiné par la technique de l'ASM: un pluton syntectonique de la transpression dextre hercynienne. Bull
763 Soc geol Fr 175: 157–174.

764 Berger GM, Fontelles M, Leblanc D, Clauzon G, Marchal JP, Vautrelle C (1993) Notice de la carte géologique
765 de la France, feuille Rivesaltes (1090), scale 1:50 000. Orléans : BRGM.

766 Bouhallier H, Choukroune P, Balleve M (1991) Evolution structurale de la croûte profonde hercynienne :
767 exemple du massif de l'agly (Pyrenees-Orientales, France). CR Acad Sci Paris 312:647-654.

768 Carreras J, Druguet E (2014) Framing the tectonic regime of the NE Iberian Variscan segment. Geol Soc Spec
769 Publ London 405. doi.org/10.1144/SP405.7

770 Casas JM, Castiñeiras P, Navidad M, Liesa M, Carreras J (2010) New insights into the Late Ordovician
771 magmatism in the Eastern Pyrenees: U–Pb SHRIMP zircon data from the Canigó massif. Gondwana Res
772 17:317-324.

773 Casas JM, Navidad M, Castiñeiras P, Liesa M, Aguilar C, Carreras J, Hofmann M, Gärtner A, Linnemann U
774 (2015) The Late Neoproterozoic magmatism in the Ediacaran series of the Eastern Pyrenees: new ages
775 and isotope geochemistry. Int J Earth Sci 104:909-925.

776 Castiñeiras P, Navidad M, Liesa M, Carreras J, Casas JM (2008) U–Pb zircon ages (SHRIMP) for Cadomian and
777 Early Ordovician magmatism in the Eastern Pyrenees: new insights into the pre-Variscan evolution of
778 the northern Gondwana margin. Tectonophysics 461:228-239.

779 Chardon D, Aretz M, Roques D (2020) Reappraisal of Variscan tectonics in the southern French Massif Central.
780 Tectonophysics 787, 228477.

781 Charles N, Faure M, Chen Y (2009) The Montagne Noire migmatitic dome emplacement (French Massif Central):
782 new insights from petro-fabric and AMS studies. *J Struct Geol* 31, 1423–1440.

783 Chelle-Michou C, Laurent O, Moyen JF et al (2017) Pre-Cadomian to late-Variscan odyssey of the eastern Massif
784 Central, France: Formation of the West European crust in a nutshell. *Gondwana Res.* 46:170-190.

785 Clark MK, Royden LH (2000) Topographic ooze: building the eastern margin of Tibet by lower crustal flow.
786 *Geology* 28, 703–706.

787 Cochelin B, Chardon D, Denèle Y, Gumiaux C, Le Bayon B (2017) Vertical strain partitioning in hot Variscan
788 crust: Syn-convergence escape of the Pyrenees in the Iberian-Armorican syntax. *Bull Soc Geol Fr* 188.
789 <https://doi.org/10.1051/bsgf/2017206>

790 Cochelin B, Lemirre B, Denèle Y, de Saint Blanquat M (2021) Strain partitioning within bending orogens, new
791 insights from the Variscan belt (Chiroulet-Lesponne domes, Pyrenees). *Tectonics*, 40, e2020TC006386.
792 <https://doi.org/10.1029/2020TC006386>

793 Couzinié S, Moyen JF, Villaros A, Paquette JL, Scarrow JH, Marignac C (2014) Temporal relationships between
794 Mg-K mafic magmatism and catastrophic melting of the Variscan crust in the southern part of Velay
795 Complex (Massif Central, France). *J Geosci* 59:1-18.

796 Cugerone A, Roger F, Cenki-Tok B, Oliot E, Paquette JL (2021) Variscan U-Th-Pb age for stratabound Pb-Zn
797 mineralization in the Bossòst dome (Pyrenean Axial Zone), *Ore Geol Rev*, 139: 104503.
798 <https://doi.org/10.1016/j.oregeorev.2021.104503>

799 de Saint Blanquat M (1993) La faille normale ductile du massif de Saint-Barthélémy. Evolution hercynienne des
800 massifs nord-pyrénéens catazonaux considérée du point de vue de leur histoire thermique. *Geodin Acta*
801 6:59-77.

802 de Saint Blanquat M, Tikoff B, Teyssier C, Vigneresse JL (1998) Transpressional kinematics and magmatic arcs.
803 In: Holdsworth RE, Strachan RA, Dewey JF (Eds.), *Continental Transpressional and Transtensional*
804 *Tectonics. Geol Soc Spec Publ*, 135:327–340.

805 Debon F, Zimmermann JL (1993) Mafic dykes from some plutons of the Western Pyrenean Axial Zone (France,
806 Spain): markers of the transition from Late-Hercynian to early Alpine events. *Schweizerische*
807 *Mineralogische und Petrographische Mitteilungen* 73:421–433.

808 Delay F (1989) Le massif nord-pyrénéen de l'Agly (Pyrénées orientales) : Évolution tectono-métamorphique et
809 exemple d'un amincissement crustal polyphasé. PhD thesis, Lille (France): Univ. Lille 1.

810 Deloule E, Alexandrov P, Cheilletz A, Laumonier B, Barbey P (2002) In-situ U–Pb zircon ages for Early
811 Ordovician magmatism in the eastern Pyrenees, France: the Canigou orthogneisses. *International Journal*
812 *of Earth Sciences* 91:398-405.

813 Denèle Y, Olivier P, Gleizes G, Barbey P (2009) Decoupling between the Middle and Upper Crust during
814 Transpression-Related Lateral Flow: Variscan Evolution of the Aston Gneiss Dome (Pyrenees, France).
815 *Tectonophysics* 477: 244–261.

816 Denèle Y, Paquette JL, Olivier P, Barbey P (2012) Permian granites in the Pyrenees: the Aya pluton (Basque
817 Country). *Terra Nova* 24:105-113.

818 Denèle Y, Laumonier L, Paquette JL, Olivier P, Gleizes G, Barbey P (2014) Timing of granite emplacement,
819 crustal flow and gneiss dome formation in the Variscan segment of the Pyrenees. *Geol Soc London Spec*
820 *Publ* 405:265-287.

821 Díez Fernández R, Pereira MF (2016) Extensional orogenic collapse captured by strike-slip tectonics: Constraints
822 from structural geology and U-Pb geochronology of the Pinhel shear zone (Variscan orogen, Iberian
823 Massif). *Tectonophysics* 691:290-310.

824 Druguet E (2001) Development of high thermal gradients by coeval transpression and magmatism during the
825 Variscan orogeny: insights from the Cap de Creus (Eastern Pyrenees). *Tectonophysics*, 332:275-293.

826 Druguet E, Castro A, Chichorro M, Pereira MF, Fernández C (2014) Zircon geochronology of intrusive rocks
827 from Cap de Creus, Eastern Pyrenees. *Geol Mag*, 151:1095-1114.

828 Dumond G, Goncalves P, Williams ML, Jercinovic MJ (2015) Monazite as a monitor of melting, garnet growth
829 and feldspar recrystallization in continental lower crust. *J Metamorph Geol* 33:735-762.

830 Edel JB, Schulmann K, Lexa O, Lardeaux JM (2018) Late Palaeozoic palaeomagnetic and tectonic constraints for
831 amalgamation of Pangea supercontinent in the European Variscan belt. *Earth Sci Rev* 177:589-612.

832 Faure M, Cocherie A, Gaché J et al. (2014) Middle Carboniferous intracontinental subduction in the Outer Zone
833 of the Variscan Belt (Montagne Noire Axial Zone, French Massif Central): multi-method
834 geochronological approach of polyphase metamorphism. In: Schulmann K, Martinez Catalan JR,
835 Lardeaux JM, Janousek V, Oggiano G (Eds.), *The Variscan Orogeny: Extent, Timescale and the*
836 *Formation of the European Crust*. Geol Soc London, Spec Publ 405. <http://dx.doi.org/10.1144/SP405.2>.

837 Fonteilles M, Guitard G, Raguin E (1964) Sur la présence de gneiss à disthène et cordiérite dans le massif du
838 Saint-Barthélémy (Pyrénées de l’Ariège). *CR Acad Sci Paris* 258:3524–3525.

839 Fonteilles M (1970) Géologie des terrains métamorphiques et granitiques du massif hercynien de l'Agly (Pyrénées
840 orientales). Bull BRGM 3:1-54.

841 Fonteilles M, Guitard G (1971) Disthène relique et disthène hystérogène dans les terrains métamorphiques
842 hercyniens des Pyrénées orientales franco-espagnoles. CR Acad Sci Paris 272:361-363.

843 Fonteilles M, Leblanc D, Clauzon G, Vaudin JL, Berger GM (1993) Carte géologique de la France, feuille
844 Rivesaltes (1090), scale 1:50 000. Orléans : BRGM.

845 Franke W (2014) Topography of the Variscan orogen in Europe: Failed—not collapsed: Int J Earth Sci, 103,
846 1471–1499, doi:10.1007/s00531-014-1014-9

847 Franke W (2017) The origin of contractional structures in extensional gneiss domes: COMMENT. Geology 45,
848 e415. <https://doi.org/10.1130/G39092C.1>.

849 Franke W, Cocks LRM, Torsvik TH (2017) The Palaeozoic Variscan oceans revisited. Gondwana Res 48:257-
850 284. <https://doi.org/10.1016/j.gr.2017.03.005>

851 Gerbault M, Martinod J, Herail G (2005) Possible orogeny-parallel lower crustal flow and thickening in the central
852 Andes. Tectonophysics, 399:59–72, doi:10.1016/j.tecto.2004.12.015.

853 Gil-Imaz A, Lago-San José M, Galé C, Pueyo-Anchuela O, Ubide T, Tierz P, Oliva-Urcia B (2012) The Permian
854 mafic dyke swarm of the Panticosa pluton (Pyrenean Axial Zone, Spain): simultaneous emplacement
855 with the late-Variscan extension. Journal of Structural Geology 42:171–183.

856 Gleizes G, Leblanc D, Bouchez JL (1998a) The main phase of the Hercynian orogeny in the Pyrenees is a dextral
857 transpression. Geol Soc London Spec Publ 135: 267–273.

858 Gleizes G, Leblanc D, Santana V, Olivier O, Bouchez JL (1998b) Sigmoidal structures featuring dextral shear
859 during emplacement of the Hercynian granite complex of Caunterets–Panticosa (Pyrenees). J Struct Geol
860 20:1229–1245.

861 Gleizes G, Leblanc D, Olivier P, Bouchez JL (2001) Strain partitioning in a pluton during emplacement in
862 transpressional regime: The Example of the Néouvielle Granite (Pyrenees). Int J Earth Sci 90: 325–340.

863 Gleizes G, Crevon G, Asrat A, Barbey P (2006) Structure, age and mode of emplacement of the Hercynian
864 Bordères-Louron pluton (Central Pyrenees, France). Int J Earth Sci 95:1039–1052.

865 Goncalves P, Nicollet C, Montel JM (2004) Petrology and in situ U–Th–Pb monazite geochronology of ultrahigh-
866 temperature metamorphism from the Andriamena mafic unit, north–central Madagascar. Significance of
867 a petrographical P–T path in a polymetamorphic context. J Petrol, 45:1923-1957.

868 Handy MR, Mulch A, Rosenau M, Rosenberg CL (2001) The role of fault zone and melts as agents of weakening,
869 hardening and differentiation of the continental crust: A synthesis, in: Holdsworth RE et al. (eds) *Nature*
870 and Tectonic Significance of Fault Zone Weakening, *Geol Soc London Spec Publ*, 186, 305–332.

871 Hawkins DP, Bowring SA (1997). U-Pb systematics of monazite and xenotime: case studies from the
872 Paleoproterozoic of the Grand Canyon, Arizona. *Contrib Mineral Petrol* 127:87-103

873 Hurai V, Paquette, JL, Huraiová M, Konečný P (2010) Age of deep crustal magmatic chambers in the intra-
874 Carpathian back-arc basin inferred from LA-ICPMS U-Th-Pb dating of zircon and monazite from
875 igneous xenoliths in alkali basalts. *J Volc Geo Res* 198:275-287.

876 Jaffey AH, Flynn KF, Glendenin LE, Bentley WC, Essling AM (1971) Precision measurement of half-lives and
877 specific activities of ²³⁵U and ²³⁸U. *Phys Rev C*4, 1889–1906.

878 Kilzi MA, Grégoire M, Bosse V, Benoit M, Driouch Y, de Saint Blanquat M, Debat P (2016) Geochemistry and
879 zircon U–Pb geochronology of the ultramafic and mafic rocks emplaced within the anatectic series of
880 the Variscan Pyrenees: The example of the Gavarnie–Heas dome (France). *C R Geosci*, 348:107-115.

881 Lago M, Arranz E, Pocoví A, Galé C, Gil-Imaz A (2004) Permian magmatism and basin dynamics in the southern
882 Pyrenees: a record of the transition from late Variscan transtension to early Alpine extension. In: Wilson
883 M, Neumann ER, Davies GR, Timmerman MJ, Heeremans M, Larsen BT (Eds.), *Permo-Carboniferous*
884 *Magmatism and Rifting in Europe*. *Geol. Soc. Lond. Spec. Publ.*, 223, pp. 439–464 (London).

885 Laurent O, Couzinié S, Zeh A, Vanderhaeghe O, Moyen JF, Villaros A, Gardien V, Chelle-Michou C (2017)
886 Protracted, coeval crust and mantle melting during Variscan late orogenic evolution: U–Pb dating in the
887 eastern French Massif Central. *Int J Earth Sci* 106:421-451.

888 Lemirre B (2016). *Origine et développement de la thermicité dans les Pyrénées varisques*. PhD thesis, Toulouse
889 (France), Univ. Toulouse.

890 Lemirre B, Cochelin B, Duchêne S, de Saint Blanquat M, Poujol M (2019) Origin and duration of late orogenic
891 magmatism in the foreland of the Variscan belt (Lesponne—Chiroulet—Neouvielle area, french
892 Pyrenees). *Lithos* 336:183-201.

893 Liesa M, Carreras J, Castiñeiras P, Casas JM, Navidad M, Vilà, M (2011) U-Pb zircon age of Ordovician
894 magmatism in the Albera Massif (Eastern Pyrenees), *Geol Acta* 9:1–9.

895 Linnemann U, Ouzegane K, Drareni A, Hofmann M, Becker S, Gärtner A, Sagawe A (2011) Sands of West
896 Gondwana: an archive of secular magmatism and plate interactions — a case study from the Cambro-

897 Ordovician section of the Tassili Ouan Ahaggar (Algerian Sahara) using U–Pb LA-ICP-MS detrital
898 zircon ages. *Lithos* 123:188–203.

899 Linnemann U, Gerdes A, Hofmann M, Marko L (2014) The Cadomian Orogen: Neoproterozoic to Early Cambrian
900 crustal growth and orogenic zoning along the periphery of the West African Craton — Constraints from
901 U–Pb Zircon Ages and Hf isotopes (Schwarzburg Antiform, Germany). *Precambrian Res* 244:236–278.

902 Lopez-Sanchez MA, Aleinikoff JN, Marcos A, Martínez FJ, Llana-Fúnez S (2016) An example of low-Th/U
903 zircon overgrowths of magmatic origin in a late orogenic Variscan intrusion: the San Ciprián massif (NW
904 Spain). *J Geol Soc* 173:282–291.

905 Lopez-Sanchez MA, García-Sanseguendo J, Martínez FJ (2019) The significance of early Permian and early
906 Carboniferous U–Pb zircon ages in the Bossòst and Lys-Caillaouas granitoids (Pyrenean Axial Zone).
907 *Geol J* 54:2048-2063.

908 Lotout C, Pitra P, Poujol M, Van Den Driessche J (2017) Ordovician magmatism in the Lévézou massif (French
909 Massif Central): tectonic and geodynamic implications. *Int J Earth Sci* 106:501-515.

910 Ludwig KR (2001) User manual for Isoplot/Ex rev. 2.49. A geochronological toolkit for Microsoft Excel.
911 Berkeley Geochronology Center Special Publication 1a, 1–56.

912 Maierová P, Schulmann K, Lexa O et al (2016) European Variscan orogenic evolution as an analogue of Tibetan-
913 Himalayan orogen: Insights from petrology and numerical modeling. *Tectonics* 35:1760–1780.

914 Maierová P, Schulmann K, Gerya T (2018) Relamination styles in collisional orogens. *Tectonics* 224–250

915 Maierova P, Schulmann K, Stípska P, Gerya T, Lexa O (2021) Trans-litospheric diapirism explains the presence
916 of ultra-high pressure rock in the European Variscides. *Commun. Earth Environ.* 2, 56.
917 <https://doi.org/10.1038/s43247-021-00122-w>.

918 Margalef A, Castiñeiras P, Casas JM, Navidad M, Liesa M, Linnemann U, Hofmann M, Gärtner A (2016) Detrital
919 zircons from the Ordovician rocks of the Pyrenees: Geochronological constraints and provenance.
920 *Tectonophysics* 681:124-134.

921 Martí J, Solari L, Casas JM, Chichorro M (2019) New late Middle to early Late Ordovician U–Pb zircon ages of
922 extension-related felsic volcanic rocks in the Eastern Pyrenees (NE Iberia): tectonic implications. *Geol*
923 *Mag*, 156:1783-1792.

924 Martínez FJ, Iriondo A, Dietsch C, Aleinikoff JN, Peucat JJ, Cirès J, Reche J, Capdevila R (2011) U-Pb SHRIMP-
925 RG zircon ages and Nd signature of lower Paleozoic rifting-related magmatism in the Variscan basement
926 of the Eastern Pyrenees. *Lithos*, 127:10-23.

927 Martínez Catalán JR, Schulmann K, Ghienne JF (2021) The Mid-Variscan Allochthon: Keys from correlation,
928 partial retrodeformation and plate-tectonic reconstruction to unlock the geometry of a non-cylindrical
929 belt. *Earth-Sci Rev* 220:103700.

930 Melleton J, Cocherie A, Faure M, Rossi P (2010) Precambrian protoliths and Early Paleozoic magmatism in the
931 French Massif Central: U–Pb data and the North Gondwana connection in the west European Variscan
932 belt. *Gondwana Res* 17:13-25.

933 Mezger J, Gerdes A (2016) Early Variscan (Visean) granites in the core of central Pyrenean gneiss domes:
934 implications from laser ablation U–Pb and Th–Pb studies. *Gondwana Res* 29:181-198.

935 Odlum ML, Stockli DF (2019) Thermotectonic evolution of the North Pyrenean Agly Massif during Early
936 Cretaceous hyperextension using multi-mineral U–Pb thermochronometry. *Tectonics*, 38.
937 doi.org/10.1029/2018TC005298

938 Olivier P, Gleizes G, Paquette JL (2004) Gneiss domes and granite emplacement in an obliquely convergent
939 regime: new interpretation of the Variscan agly massif (eastern Pyrenees, France), *Geol. Soc. Am. sp.*
940 *pap.* 380:229-240.

941 Olivier P, Gleizes G, Paquette JL Muñoz Sáez C (2008) Structure and U–Pb Dating of the Saint-Arnac Pluton and
942 the Ansignan Charnockite (Agly Massif): A Cross-Section from the Upper to the Middle Crust of the
943 Variscan Eastern Pyrenees. *J Geol Soc* 165:141-52.

944 Paquet J, Mansy JL (1991) The structure of the Eastern Pyrenees (transect of the Agly massif): an example of
945 crustal thinning. *CR Acad Sci Paris* 312:913-919.

946 Paquette JL, Tiepolo M (2007) High resolution (5 μm) U–Th–Pb isotopes dating of monazite with excimer laser
947 ablation (ELA)-ICPMS. *Chem Geol*, 240, 222-237.

948 Paquette JL, Piro, JL Devidal JL, Bosse V, Didier A (2014). Sensitivity enhancement in LA-ICP-MS by N2
949 addition to carrier gas: application to radiometric dating of U–Th-bearing minerals. *Agilent ICP-MS J*
950 *58*, 4–5.

951 Paquette JL, Barbey P, Olivier P (2021) Âge ordovicien moyen et caractéristiques chimiques du gneiss de la
952 Rivérole (Massif de l'Agly, Pyrénées orientales). *Bull Soc Hist nat Toulouse* 156:111-119

953 Pereira MF, Castro A, Chichorro M, Fernández C, Diaz-Alvarado J, Martí J, Rodríguez C (2014) Chronological
954 link between deep-seated processes in magma chambers and eruptions: Permo-Carboniferous
955 magmatism in the core of Pangaea (Southern Pyrenees). *Gondwana Res* 25:290-308.

956 Pereira MF, Díez Fernández R, Gama C, Hofmann M, Gärtner A, Linnemann U (2018) S-type granite generation
957 and emplacement during a regional switch from extensional to contractional deformation (Central Iberian
958 Zone, Iberian autochthonous domain, Variscan Orogeny). *Int J Earth Sci* 107:251-267.

959 Pereira MF, Fuenlabrada JM, Rodríguez C, Castro A (2022) Changing Carboniferous Arc Magmatism in the Ossa-
960 Morena Zone (Southwest Iberia): Implications for the Variscan Belt. *Minerals* 12:597.

961 Pin C, Lancelot J (1982) U-Pb dating of an early Paleozoic bimodal magmatism in the French Massif Central and
962 of its further metamorphic evolution. *Contrib Mineral Petrol* 79:1-12.

963 Pitra P, Poujol M, Van Den Driessche J, Bretagne E, Lotout C, Cogné N (2021) Late Variscan (315 Ma)
964 subduction or deceiving zircon REE patterns and U-Pb dates from migmatite-hosted eclogites?
965 (Montagne Noire, France). *J Metamorph Geol*, in press. <https://doi.org/10.1111/jmg.12609>

966 Poitrenaud T, Poujol M, Augier R, Marcoux E (2020) The polyphase evolution of a late Variscan W/Au deposit
967 (Salau, French Pyrenees): insights from REE and U/Pb LA-ICP-MS analyses. *Mineral Deposita* 55:1127-
968 1147.

969 Postaire B (1982) Systématique Pb commun et U-Pb sur zircons: Applications aux roches de haut grade
970 métamorphique impliquées dans la chaîne hercynienne (Europe de l'ouest) et aux granulites de Laponie
971 (Finlande). *Mémoires de la Société Géologique et Minéralogique de Bretagne* 15:29–72.

972 Rabin M, Trap P, Carry N, Fréville K, Cenki-Tok B, Lobjoie C, Goncalves P, Marquer D (2015) Strain partitioning
973 along the anatectic front in the Variscan Montagne Noire massif (Southern French Massif Central).
974 *Tectonics* 34:1709–1735.

975 Respaut JP, Lancelot JR (1983) Datation de la mise en place synmétamorphe de la charnockite d'Ansignan (massif
976 de l'Agly) par la méthode U/Pb sur zircons et monazites. *Neues Jahrb Mineral Abh* 147:21-34.

977 Rey PF, Teyssier C, Whitney DL (2010) Limit of channel flow in orogenic plateaux. *Lithosphere*, 2:328-332.

978 Rey PF, Teyssier C, Kruckenberg SC, Whitney DL (2011) Viscous collision in channel explains double domes in
979 metamorphic core complexes. *Geology* 39:387-390.

980 Rey PF, Mondy L, Duclaux G, Teyssier C, Whitney DL, Bocher M, Prigent C (2017) The origin of contractional
981 structures in extensional gneiss domes. *Geology* 45:263-266.

982 Rodríguez C, Pereira MF, Castro A, Gutiérrez-Alonso G, Fernández C (2022) Variscan intracrustal recycling by
983 melting of Carboniferous arc-like igneous protoliths (Évora Massif, Iberian Variscan belt). *GSA Bulletin*
984 134:1549-1570.

- 985 Rodríguez-Méndez L, Cuevas J, Esteban JJ, Tubía JM, Sergeev S, Larionov A (2014) Age of the magmatism
986 related to the inverted Stephanian–Permian basin of the Sallent area (Pyrenees). *Geol Soc, London, Spec*
987 *Publ* 394:101-111.
- 988 Roger F, Respaut JP, Brunal M, Matte P, Paquette JL (2004) Première datation U–Pb des orthogneiss ocellés de
989 la zone axiale de la Montagne noire (Sud du Massif central) : nouveaux témoins du magmatisme
990 ordovicien dans la chaîne Varisque. *CR Geosci* 336:19-28.
- 991 Roger F, Teyssier C, Respaut JP et al (2015) Timing of formation and exhumation of the Montagne Noire double
992 dome, French Massif Central. *Tectonophysics* 640-641:53-69.
- 993 Roger F, Teyssier C, Whitney DL, Respaut JP, Paquette JL, Rey PF (2020) Age of metamorphism and deformation
994 in the Montagne Noire dome (French Massif Central): Tapping into the memory of fine-grained gneisses
995 using monazite U-Th-Pb geochronology. *Tectonophysics* 776. doi.org/10.1016/j.tecto.2019.228316
- 996 Román-Berdiel T, Casas AM, Oliva-Urcia B, Pueyo EL, Liesa C, Soto R (2006) The Variscan Millares granite
997 (central Pyrenees): Pluton emplacement in a T fracture of a dextral shear zone. *Geodin Acta* 19: 197–
998 211.
- 999 Schnapperelle S, Mezger JE, Stipp M, Hofmann M, Gärtner A, Linnemann U (2020) Polyphase magmatic pulses
1000 along the Northern Gondwana margin: U-Pb zircon geochronology from gneiss domes of the Pyrenees.
1001 *Gondwana Res* 81:291-311.
- 1002 Schulmann K, Lexa O, Stipska P et al. (2008) Vertical extrusion and horizontal channel flow of orogenic lower
1003 crust: key exhumation mechanisms in large hot orogens? *J Metamorph Geol* 26:273–297.
- 1004 Schulmann K, Catalán JRM, Lardeaux JM, Janousek V, Oggiano G (2014) The Variscan orogeny: extent,
1005 timescale and the formation of the European crust. *Geol. Soc. Lond. Spec. Publ.* 405: 1–6.
- 1006 Siron G, Goncalves P, Marquer D, Pierre T, Paquette JL, Vanardois J (2020) Contribution of magmatism, partial
1007 melting buffering and localized crustal thinning on the late-Variscan thermal structure of the Agly massif
1008 (French Pyrenees). *J Metamorph Geol* 38: 799-829
- 1009 Steiger RH, Jäger E (1977) Subcommittee on geochronology: convention on the use of decay constants in geo-
1010 and cosmochronology. *Earth Planet Sci Lett* 36:359–362
- 1011 Stephan T, Kroner UWE, Romer RL (2019) The pre-orogenic detrital zircon record of the Peri-Gondwanan crust.
1012 *Geol Mag* 156-281-307.

1013 Teipel U, Eichhorn R, Loth G, Rohrmüller J, Höll R, Kennedy A (2004) U-Pb SHRIMP and Nd isotopic data
1014 from the western Bohemian Massif (Bayerischer Wald, Germany): implications for upper Vendian and
1015 lower Ordovician magmatism. *Int J Earth Sci* 93:782-801.

1016 Tournaire Guille B, Olivier P, Paquette JL, Bosse V, Guillaume D (2019) Evolution of the middle crust of the
1017 Pyrenees during the Paleozoic: new data on the plutonic rocks from the North Pyrenean Agly Massif. *Int*
1018 *J Earth Sci* 108:245-265.

1019 Townsend KJ, Miller CF, D'Andrea JL, Ayers JC, Harrison TM, Coath CD (2000). Low temperature replacement
1020 of monazite in the Ireteba granite, southern Nevada: geochronological implications. *Chem Geol* 172:95-
1021 112

1022 Trap P, Roger F, Cenki-Tok B, Paquette JL (2017) Timing and duration of partial melting and magmatism in the
1023 Variscan Montagne Noire gneiss dome (French Massif Central). *Int J Earth Sci* 106:453–476.

1024 Vacherat A, Mouthereau F, Pik R et al (2017) Rift-to-collision sediment routing in the Pyrenees: A synthesis from
1025 sedimentological, geochronological and kinematic constraints. *Earth Sci Rev* 172:43-72.

1026 van Achterbergh E, Ryan CG, Jackson SE, Griffin WL (2001) Data reduction software for LA-ICP-MS. In:
1027 Sylvester P (ed) *Laser ablation-ICPMS in the earth science*. Mineralogical Association of Canada. Vol.
1028 29, 239-243.

1029 Van Lichtervelde M, Grand'Homme A, de Saint-Blanquat M, Olivier P, Gerdes A, Paquette JL, Melgarejo JC,
1030 Druguet E, Alfonso, P. (2017). U-Pb geochronology on zircon and columbite-group minerals of the Cap
1031 de Creus pegmatites, NE Spain. *Mineral petrol* 111:1-21.

1032 Vanardois J, Trap P, Goncalves P et al (2020) Kinematics, deformation partitioning and late Variscan magmatism
1033 in the Agly massif, Eastern Pyrenees, France. *Bull Soc Geol Fr* 191. doi.org/10.1051/bsgf/2020009

1034 Vanderhaeghe O, Laurent O, Gardien, V et al (2020) Flow of partially molten crust controlling construction,
1035 growth and collapse of the Variscan orogenic belt: the geologic record of the French Massif Central. *Bull*
1036 *Soc Géol Fr* 191, doi.org/10.1051/bsgf/2020013.

1037 Vielzeuf D (1984) Relations de phases dans le faciès granulite et implications géodynamiques. L'exemple des
1038 granulites des Pyrénées. State thesis, Clermont-Ferrand (France): Univ. Blaise Pascal.

1039 Vielzeuf D, Paquette JL, Clemens JD, Stevens G, Gannoun A, Suchorski K, Saúl A (2021) Age, duration and
1040 mineral markers of magma interactions in the deep crust: an example from the Pyrenees. *Contrib Mineral*
1041 *Petrol*. doi.org/10.1007/s00410-021-01789-2

1042 Von Raumer JF, Stampfli GM, Arenas R, Martínez SS (2015) Ediacaran to Cambrian oceanic rocks of the
1043 Gondwana margin and their tectonic interpretation. *Int J Earth Sci* 104:1107–1121.
1044 Whitney DL, Teyssier C, Rey P, Buck WR (2013) Continental and oceanic core complexes. *GSA Bulletin*
1045 125:273-298.
1046 Whitney DL, Roger F, Teyssier C, Rey PF, Respaut JP. 2015. Syncollapse eclogite metamorphism and
1047 exhumation of deep crust in a migmatite dome: The P–T–t record of the youngest Variscan eclogite
1048 (Montagne Noire, French Massif Central). *Earth Planet Sci Lett* 430: 224–234
1049 Whitney DL, Hamelin C, Teyssier C, Raia NH, Korchinski MS, Seaton NC, von der Handt A, Roger F, Rey, PF.
1050 2020. Deep crustal source of gneiss dome revealed by eclogite in migmatite (Montagne Noire, French
1051 Massif Central). *J Metamorph Geol* 38:297-327.

1052

1053 **Figures captions:**

1054 **Fig. 1 a** Paleogeographic reconstruction of the Variscan Belt during Late Carboniferous modified from
1055 Cochelin et al. (2021). **b** Simplified cross-section from the southern edge of the French Central Massif
1056 showing the lateral flow of the partially molten crust, modified from Vanderhaeghe et al. (2020). FCM:
1057 French Central Massif; MN: Montagne Noire; NPF: North Pyrenean Fault; NPZ: North Pyrenean Zone;
1058 PAZ: Pyrenean Axial Zone.

1059 **Fig. 2** Geological map of the Agly massif with localisation of the dated samples.

1060 **Fig. 3 a** Structural map and **b** cross-sections of the Agly massif modified from Vanardois et al. (2020).
1061 Dated samples are located on the map and cross-sections.

1062 **Fig. 4** Structural evidence of D1, D2 and D3 planar fabrics in the Agly massif. S1 foliations affected
1063 by F2 folds **a** in the migmatitic basement and **b** in the schists. **c** and **d** C-S structures showing top-to-
1064 the-north kinematics in high-D2 strain domains from the migmatitic basement. S2 foliations affected
1065 by F3 folds with S3 vertical axial planes **e** in gneiss and **f** in anatectic micaschists.

1066 **Fig. 5 a** Monazite U-Th-Pb concordia diagram and **b** zircon U-Pb Tera Wasserburg diagram obtained
1067 by LA-ICPMS on the Vivier leucogranite (Ag57). Error ellipses and uncertainties in ages are $\pm 2\sigma$.

1068 Dotted ellipses are not taken into account for the age calculation. $MSWD_{(C+E)}$: Mean Square of
1069 Weighted Deviates for Concordance and Equivalence.

1070 **Fig. 6** Locations and morphologies in BSE images of monazite from the Dam migmatitic paragneiss
1071 (Ag3B). **a** Thin section of the dam migmatitic paragneiss (Ag3B) with the three textural domains where
1072 monazite grains are located: **b** in the matrix, **c** and **d** within the garnet, **e** and **f** in the deformed zone.
1073 Red circles indicate laser spot analyses with a diameter of 12 μm and red numbers correspond to single-
1074 analysis concordia age obtained on the different monazite analysed (in white the grain numbers). The
1075 data reported in Table S3.

1076 **Fig. 7** Monazite U-Th-Pb concordia diagrams of the Dam migmatitic paragneiss Ag3B. Monazite grains
1077 within **a** the matrix, **b** the garnet, **c** the deformed zone and **d** all data. Error ellipses and uncertainties on
1078 ages are $\pm 2\sigma$. Dotted ellipses are not taken into account only for the age calculation.

1079 **Fig. 8** Field relations of the Brosse Ravine pegmatites (Ag03 and Ag38). **a** Cross-section passing by
1080 the boundary of the infra- and suprastructure marked by the Caladroy Shear Zone (CSZ), location on
1081 Fig. 2 and 3A. **b** Cross-section of the Brosse Ravine. Outcrop photographs of the Brosse ravine
1082 pegmatites: **c** Ag03 cross-cutting S2 foliations and bearing a xenolith of micaschist and **d** Ag38 with
1083 L2 stretching lineation marked by tourmalines (RHR orientation).

1084 **Fig. 9** Monazite U-Th-Pb concordia diagrams (**a** and **c**) and zircon Tera Wasserburg diagrams (**b** and
1085 **d**) of the Brosse ravine pegmatites Ag03 and Ag38. Error ellipses and uncertainties in ages are $\pm 2\sigma$. In
1086 the **a**, **c** and **d** diagrams, the dotted ellipses are taken into account for the concordia age calculation
1087 while in diagram **b** these are the white ellipses.

1088 **Fig. 10** Zircon U-Pb Tera Wasserburg diagram obtained by LA-ICPMS on the Planèzes pegmatite
1089 (Ag47). Error ellipses and uncertainties in ages are $\pm 2\sigma$. Dotted ellipses are not taken into account for
1090 the age calculation.

1091 **Fig. 11** Microphotographs and field relations from samples within the D3 corridor and from the two
1092 Tournefort dykes. **a** Foliations map of the Tournefort area modified from Vanardois et al. (2020). S4 is

1093 a local planar fabric induced by the emplacement of the Saint-Arnac pluton. **b** Outcrop photograph from
1094 the Tournefort pegmatite (Ag08) and its relation with de Proto-S3 magmatic foliation of the Tournefort
1095 diorite. **c** Leucogranite dyke (Ag06) thin section showing no marked deformation. *Kfs*: K-feldspar –
1096 *Qtz*: quartz – *Grt*: garnet – *Bt*: biotite – *Ms*: muscovite – *Pl*: plagioclase – *Myr*: myrmekite – *Sill*:
1097 sillimanite.

1098 **Fig. 12** Monazite U-Th-Pb concordia diagrams (**a** and **c**) and zircon Tera Wasserburg diagrams (**b** and
1099 **d**) of the Tournefort pegmatite (Ag08) and of the Tournefort leucogranite (Ag06). Error ellipses and
1100 uncertainties on ages are $\pm 2\sigma$. Dotted ellipses are not taken into account only for the age calculation.
1101 In **a** and **c**, Mn 13 and Mn10 are not plotted because they are outside the ranges, respectively.

1102 **Fig. 13 a** Monazite U-Th-Pb concordia diagram and **b** zircon U-Pb Tera Wasserburg a diagram obtained
1103 by LA-ICPMS on the Vivier orthogneiss (Ag48). Error ellipses and uncertainties in ages are $\pm 2\sigma$. White
1104 ellipses are discordant data and are not taken into account in the histogram diagram and for the age
1105 calculation, while dotted ellipses are not taken into account only when calculating the concordia age.

1106 **Fig. 14 a** Ag51 Latour-de-France Leucogranite thin section presenting myrmekites, plastic quartz
1107 deformation and recrystallization. **b** Monazite U-Th-Pb concordia diagram and **c** zircon Tera
1108 Wasserburg diagram of the Latour-de-France leucogranite (Ag51). Error ellipses and uncertainties on
1109 ages are $\pm 2\sigma$. Dotted ellipses are not taken into account only for the age calculation.

1110 **Fig. 15** Compilation of ages from the Agly massif constraining deformations and/or metamorphism and
1111 tectonic evolution. References: (1) Tournaire Guille et al. 2019; (2) Olivier et al. 2004; (3) Postaire
1112 1982; (4) Respaut and Lancelot 1983; (5) Siron et al. 2020; (6) Olivier et al. 2008; (7) This study.
1113 Geochronological data from Odium and Stockli (2019) were not processed to decipher Variscan
1114 tectonics and are not included in this compilation. *Basic Ansi. charno. facies*: Basic Ansignan
1115 charnockite facies – *Leuco. Ansi. charno. facies*: Leucocrate Ansignan charnockite facies.

1116 **Fig. 16** Tectonic model showing the strain partitioning between D2 extensive structures and D3 dextral
1117 wrenching between 325 and 300 Ma. **a** Beginning of D2 deformation in suprasolidus conditions

1118 associated to horizontal flow of the lower crust around 325 Ma forming a S2 foliation transposing
1119 former S1 foliation. **b** Beginning of the strain partitioning between the extensive S2 and C2 structures
1120 and the early proto-D3 dextral wrenching draining the Tournefort diorite. **c** Ongoing melt draining in
1121 the D3 dextral wrenching forms the Saint-Arnac granite, inducing local strain interference preserving
1122 proto-S3 foliations in the Tournefort area and localizing late-D2 at its edges. In **b** and **c**, the Tournefort
1123 diorite and Saint-Arnac granite are duplicated to illustrate 3D geometry.

1124 **Fig. 17** Tectonic evolution of the southern edge of the Variscan orogenic plateau. **a** A lateral gravity-
1125 driven flow of the molten infrastructure (in orange) below the suprastructure (in blue) took place from
1126 the French Central Massif (FCM) to the Pyrenees between ca. 325 and 310 Ma. **b** Around 308 Ma, the
1127 pervasive transcurrent deformation in the PAZ and MN reoriented the flow of the infrastructure, while
1128 in low-transcurrent domains, i.e. NPZ and FCM, the gravity driven flow continued. **c** At ca. 300 Ma,
1129 most of the anatectic melts of the infrastructure crystallized and the flow of the infrastructure stopped.
1130 The transcurrent setting was active until ca. 290 Ma with numerous dextral shear zones in the PAZ and
1131 MN, and local ones in the NPZ and FCM. See text for details.

1132 **Table 1:** Summary of geographic location, rock types, and U-Th-Pb geochronological results for
1133 samples analysed in this study. (Zr): zircon age; (Mn): monazite age; T.S.: monazite age obtained on
1134 thin section.

1135

1136 **Supplementary material**

1137 **Table S1:** Operating conditions and instrument settings for LA-ICPMS U-Th-Pb analyses.

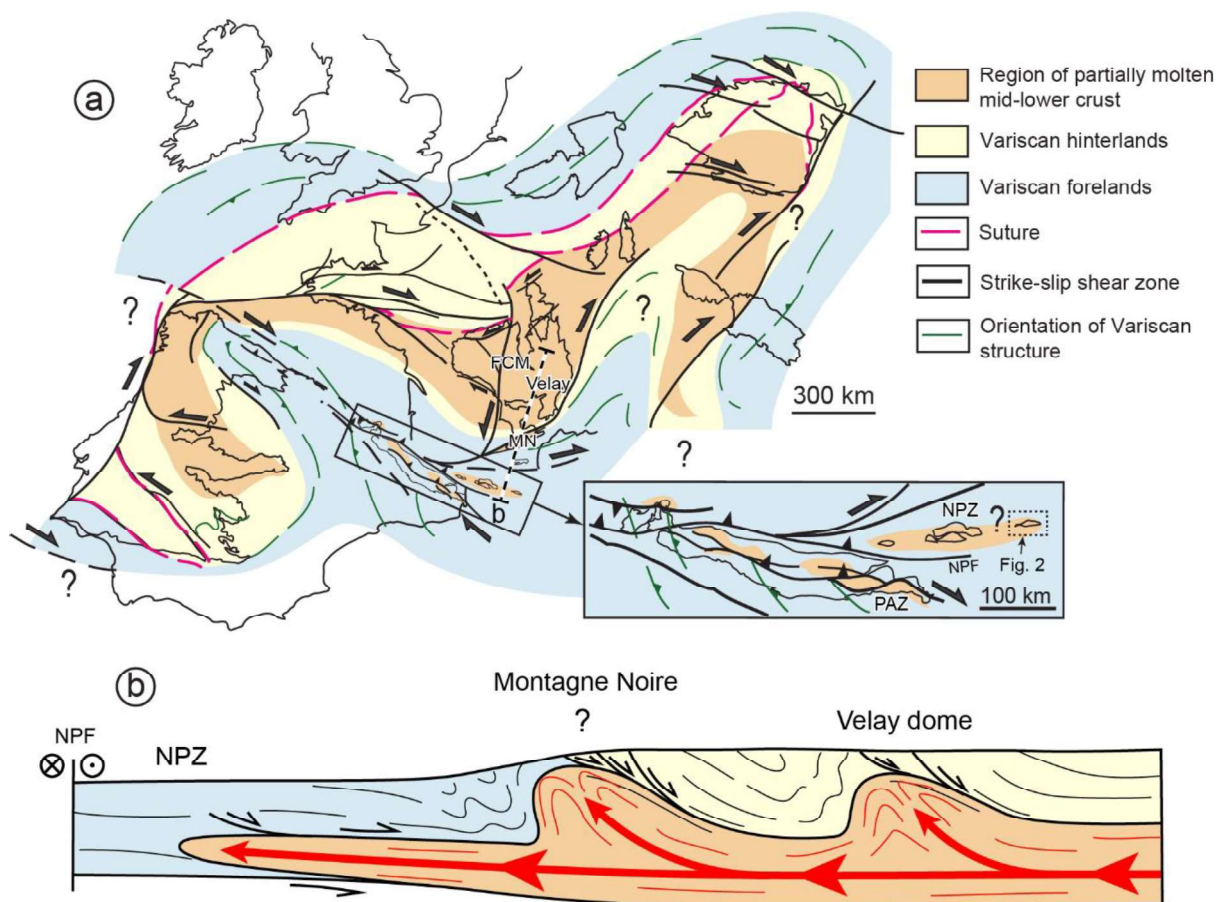
1138 **Table S2:** Analytical results of LA-ICPMS U-Th-Pb dating on monazite. Mn: monazite; R: rim; C:
1139 centre. Errors quoted in absolute values. Textural position of monazite analyzed in situ (T.S., thin
1140 section) from sample Ag3B. in Bt: included in biotite; in Sill.: included in sillimanite; in matrix:
1141 included in the quartzo-feldspathic matrix.

1142 **Table S3:** Analytical results of LA-ICPMS U-Pb dating on zircon. Zr: zircon; R: rim; C: centre.

1143 **Fig. S1:** Monazite morphologies in BSE images. Red circles indicate laser spot locations and $^{208}\text{Pb}/^{232}\text{Th}$
1144 age without error associated.

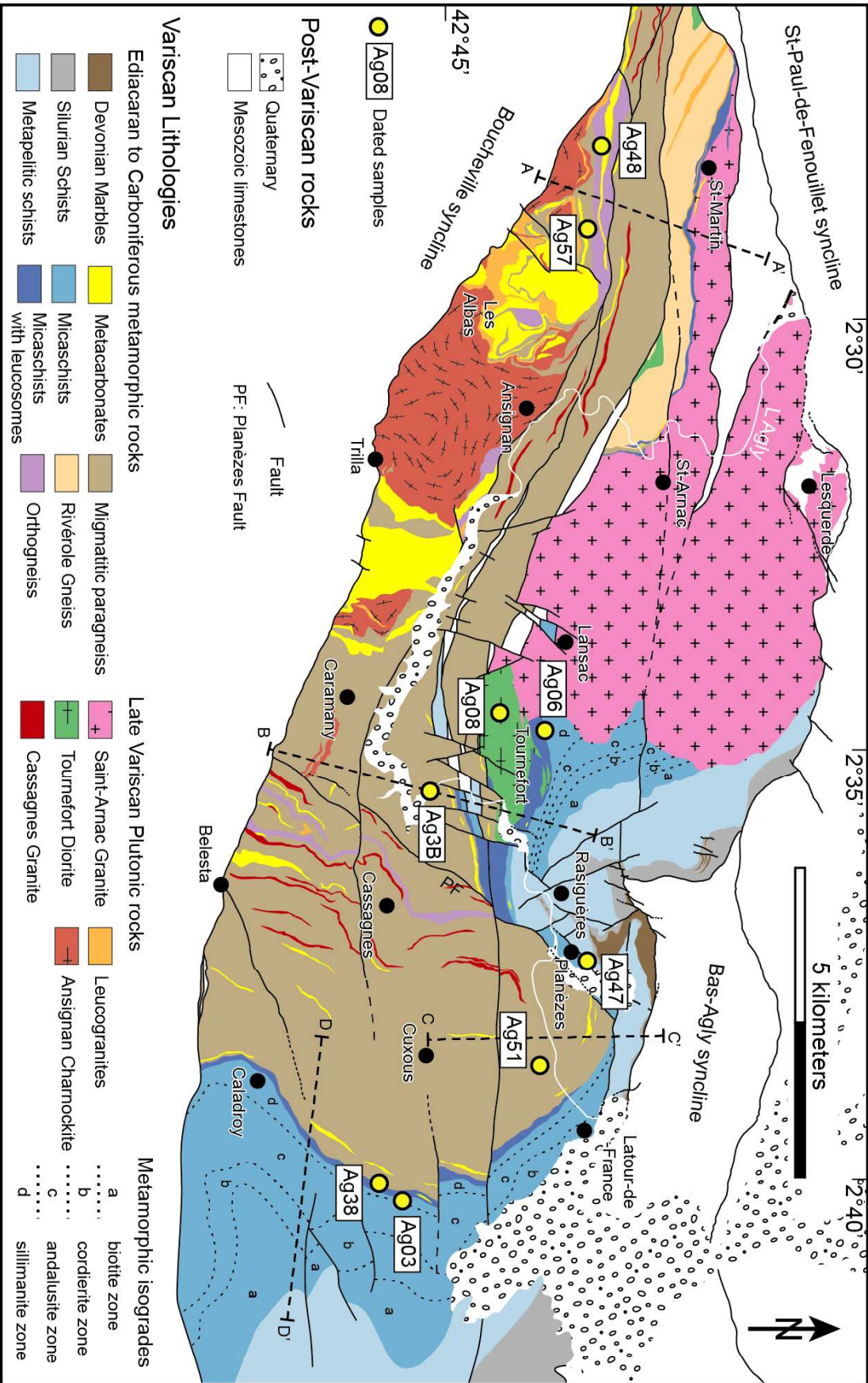
1145 **Fig. S2:** Zircon morphologies in CL images for Ag57, Ag48, Ag47, Ag51, Ag38 and Ag03, and in BSE
1146 images for Ag06 and Ag08. Red circles indicate laser spot locations and age without errors associated.

1147



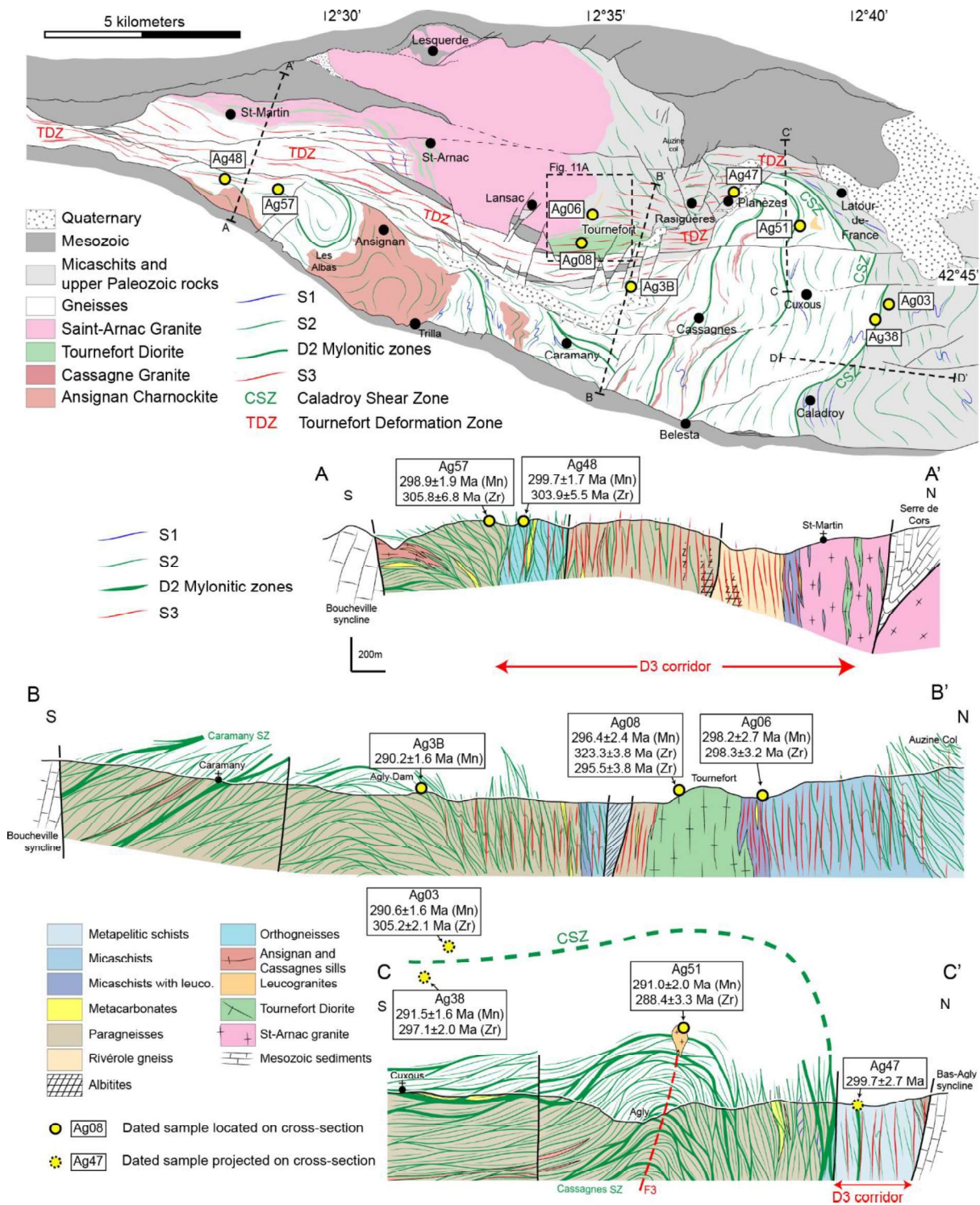
1148

1149 Fig. 1



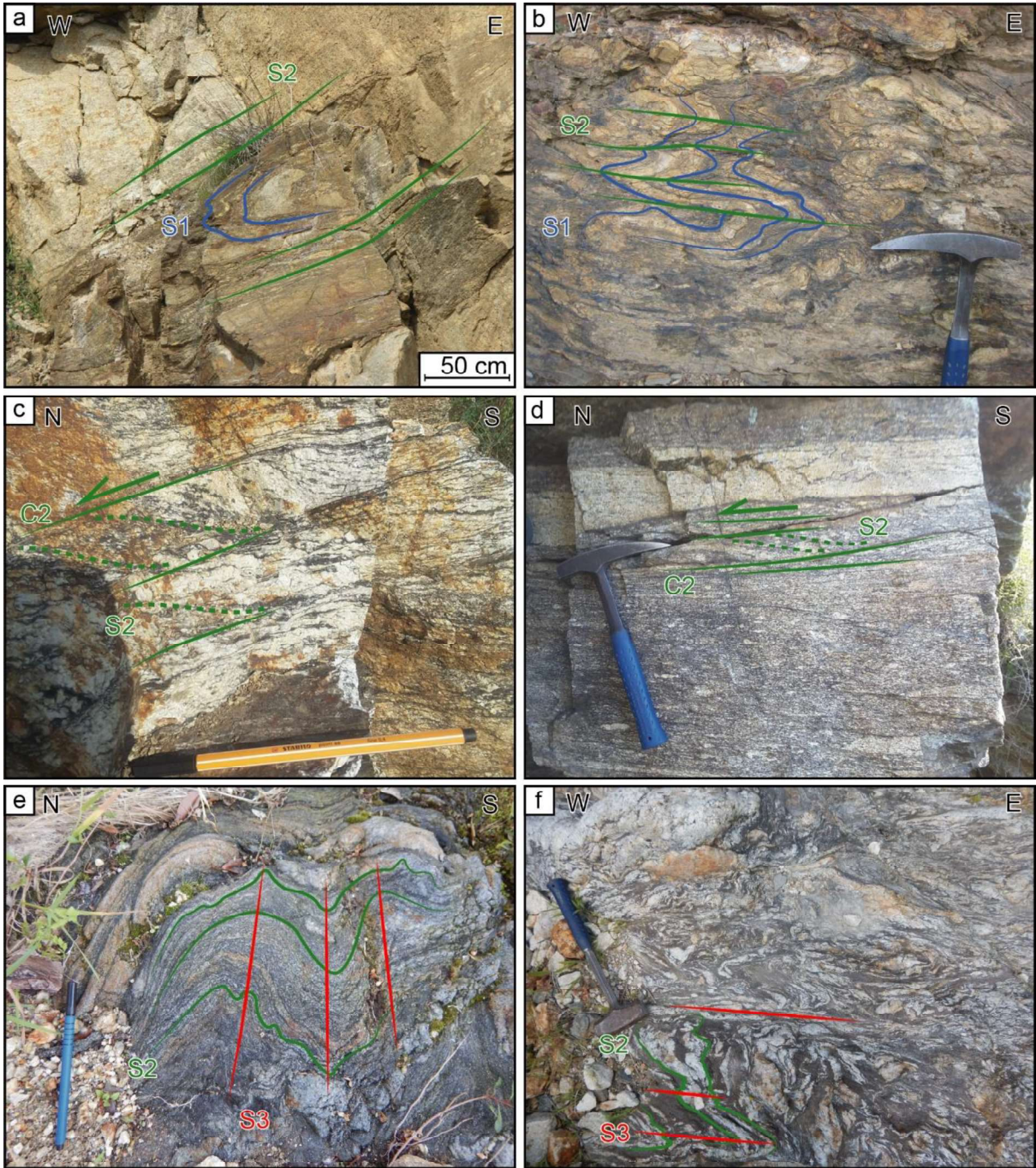
1150

1151 Fig. 2



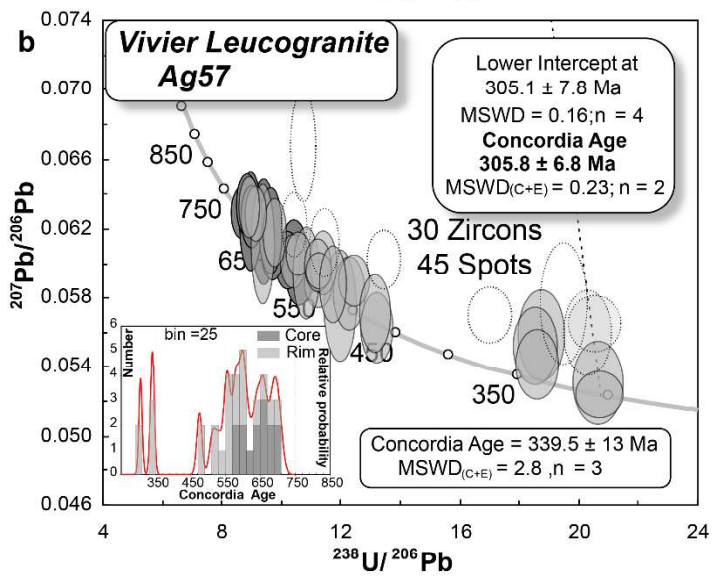
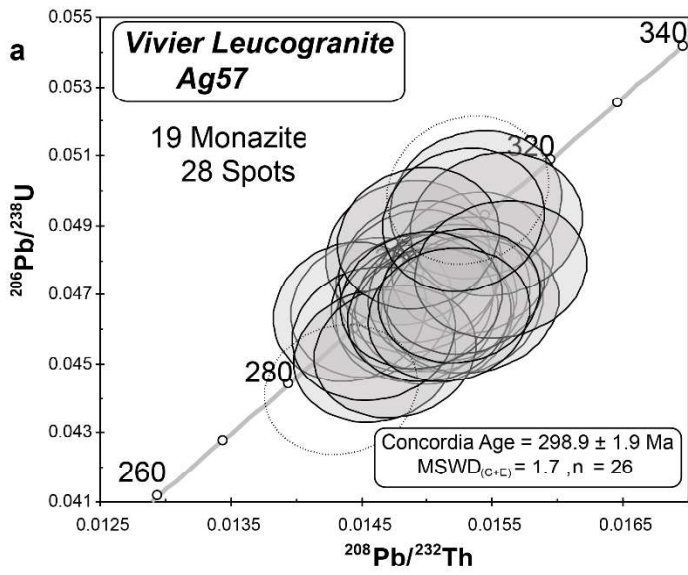
1152

1153 Fig. 3



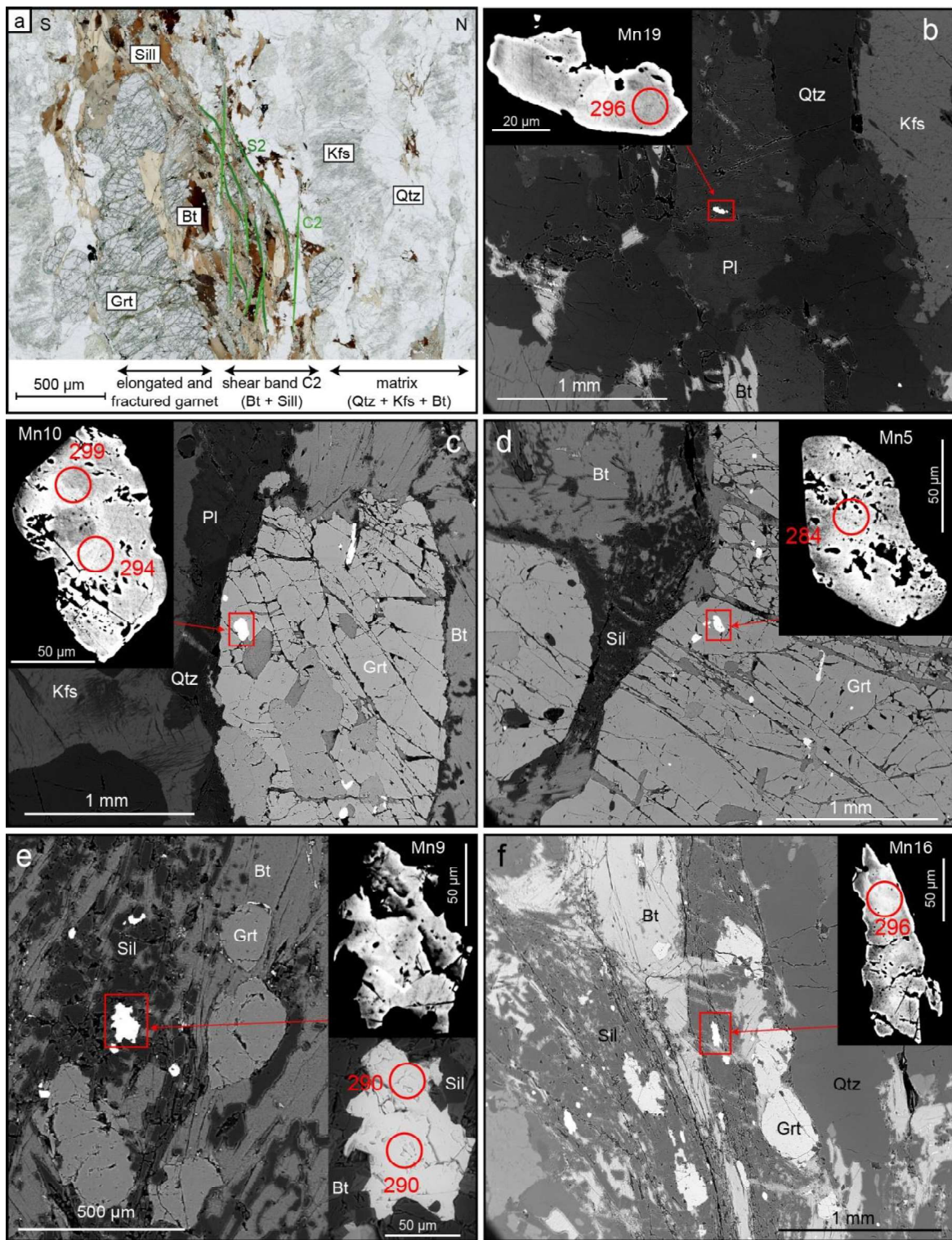
1154

1155 Fig. 4



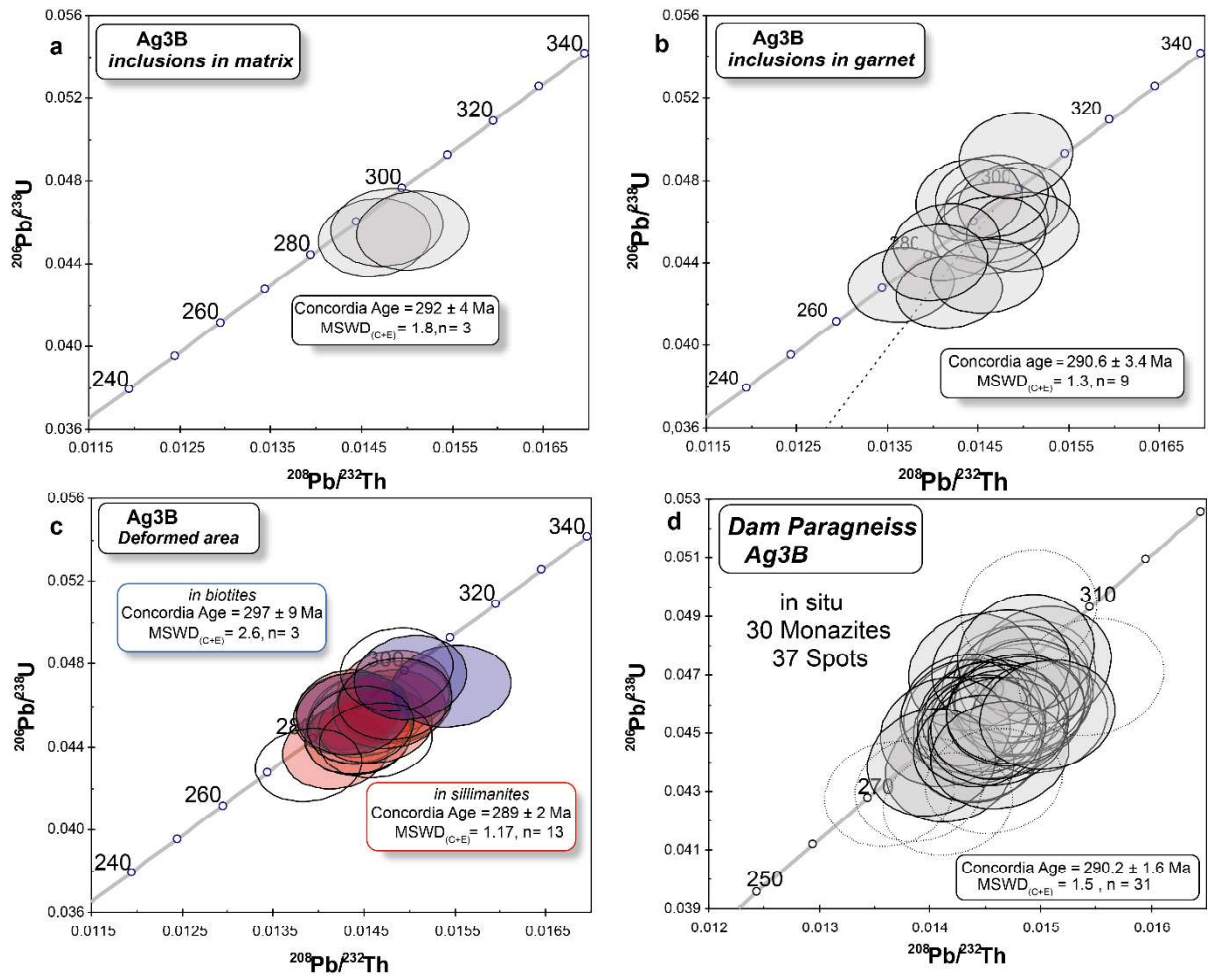
1156

1157 Fig. 5



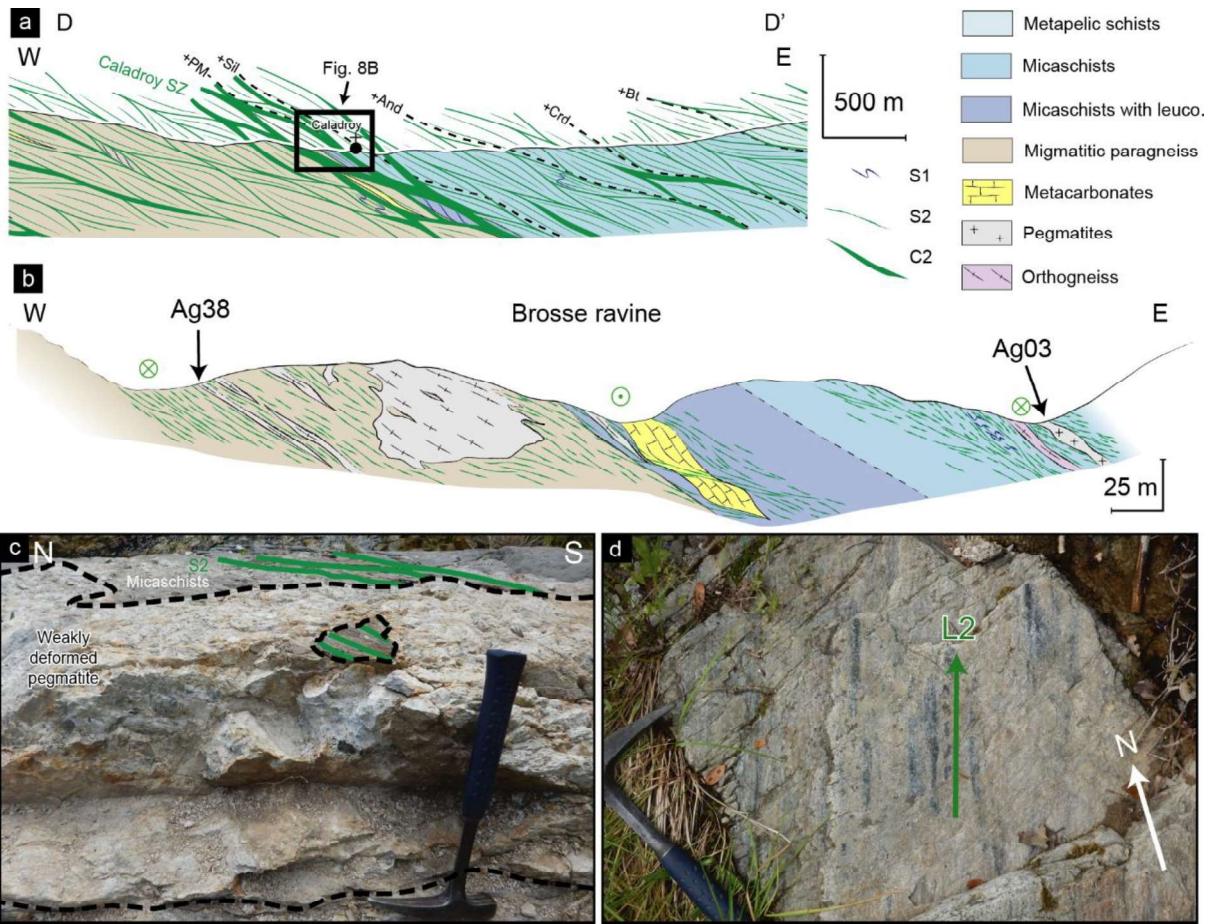
1158

1159 Fig. 6



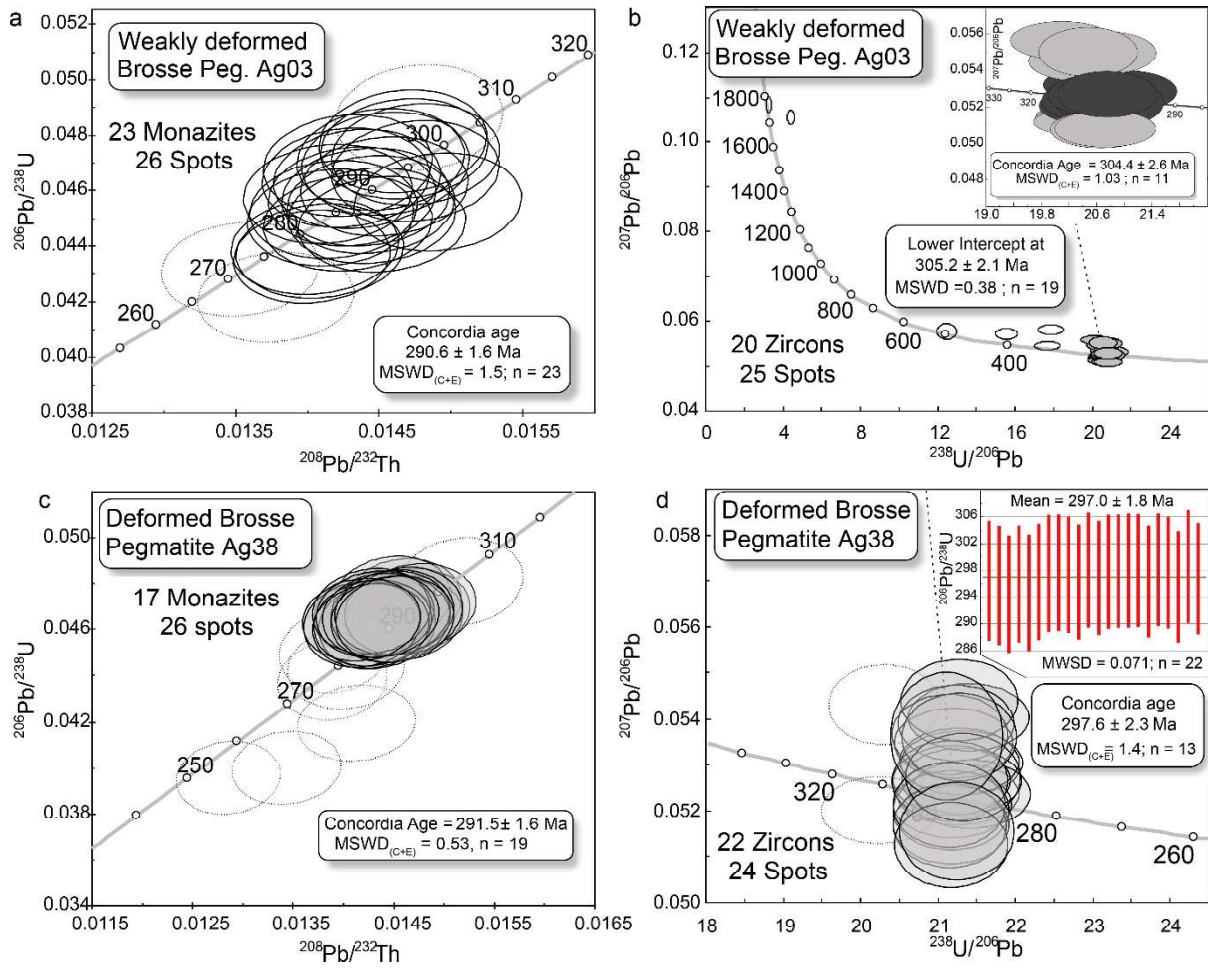
1160

1161 Fig. 7



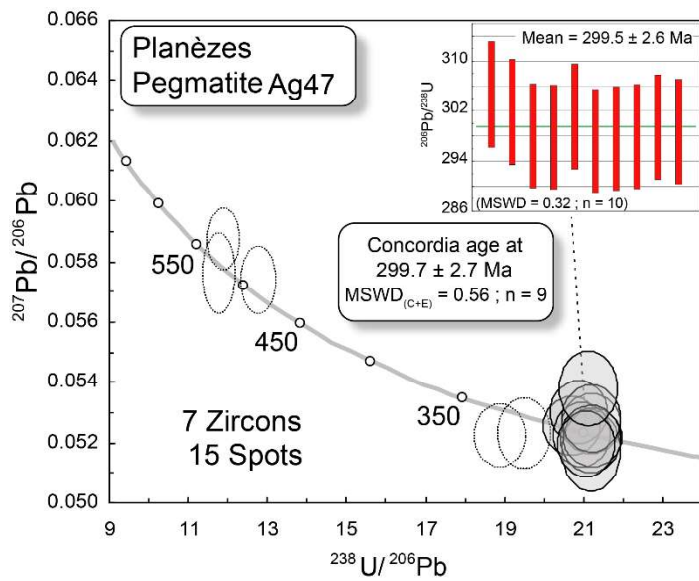
1162

1163 Fig. 8



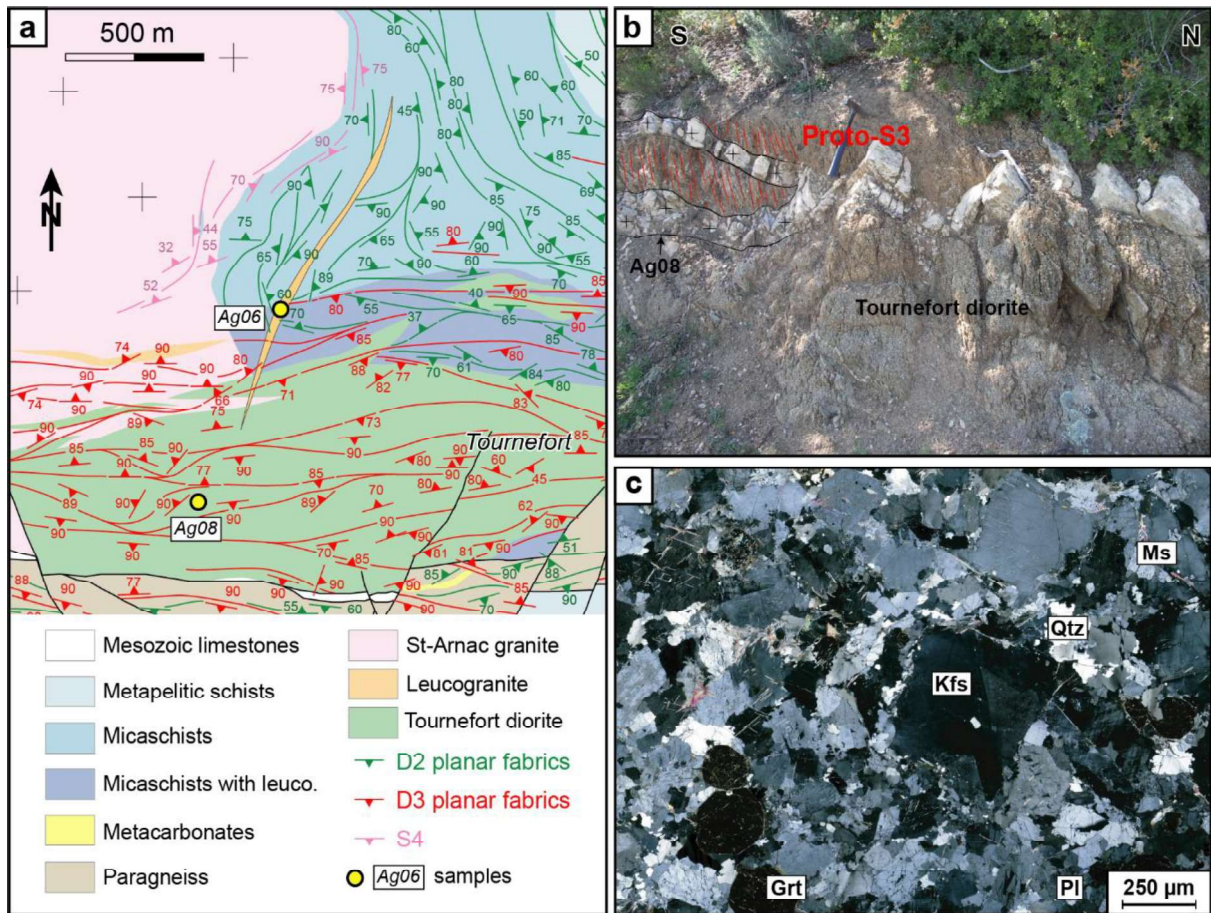
1164

1165 Fig. 9



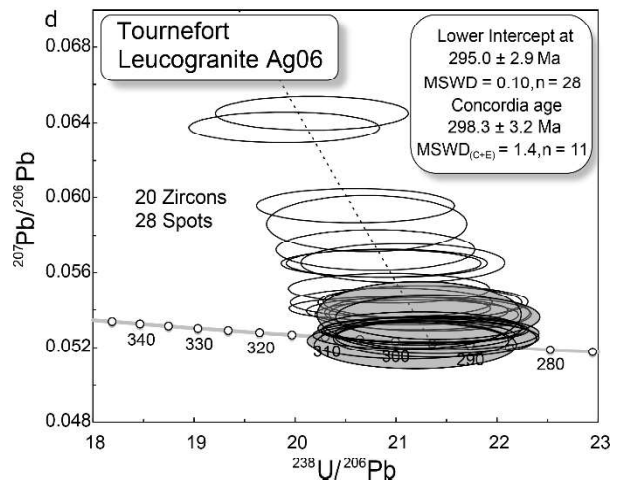
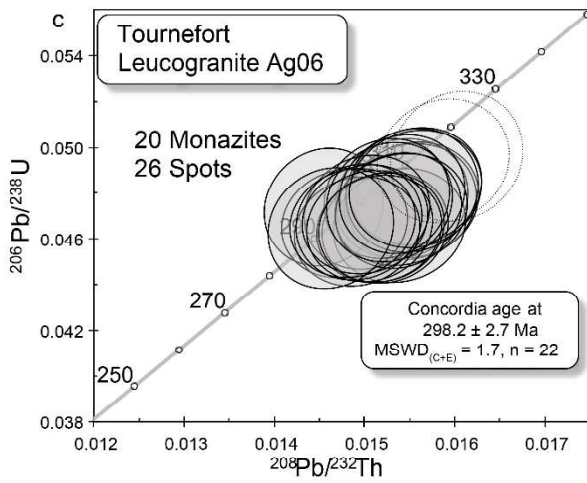
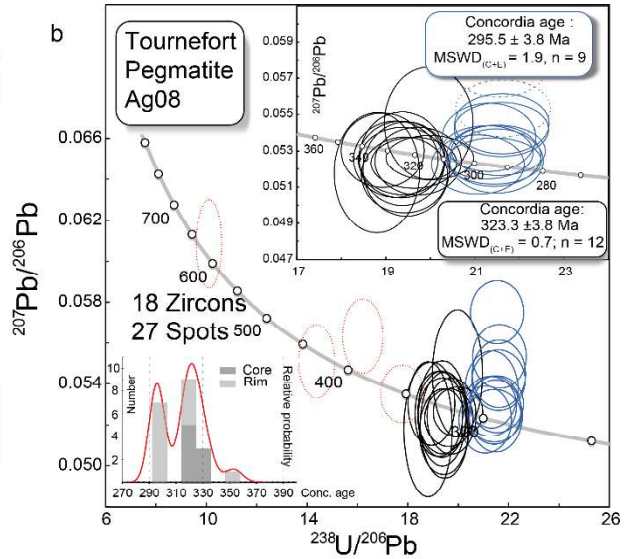
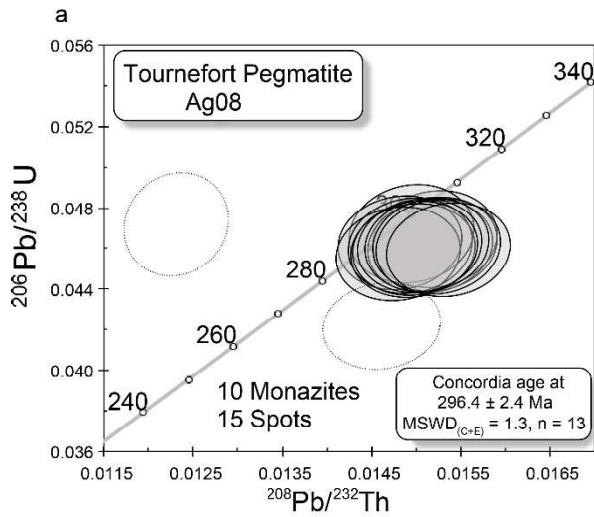
1166

1167 Fig. 10



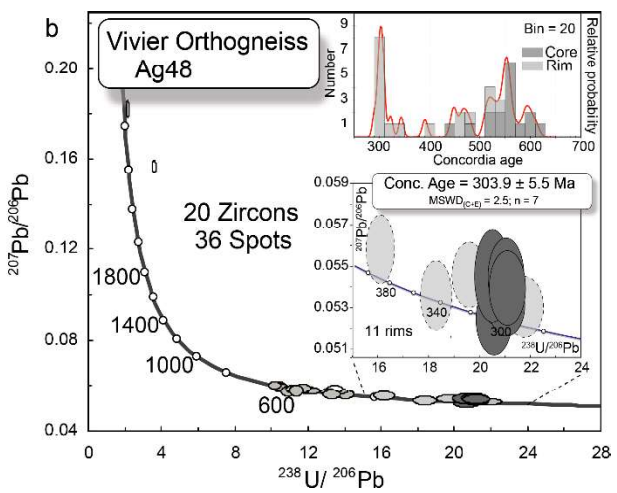
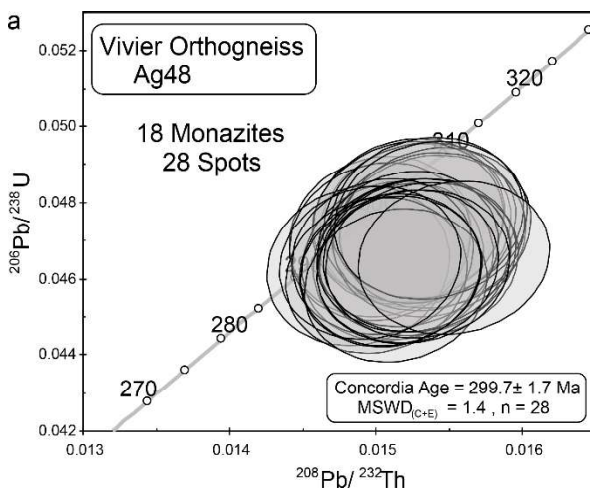
1168

1169 Fig. 11



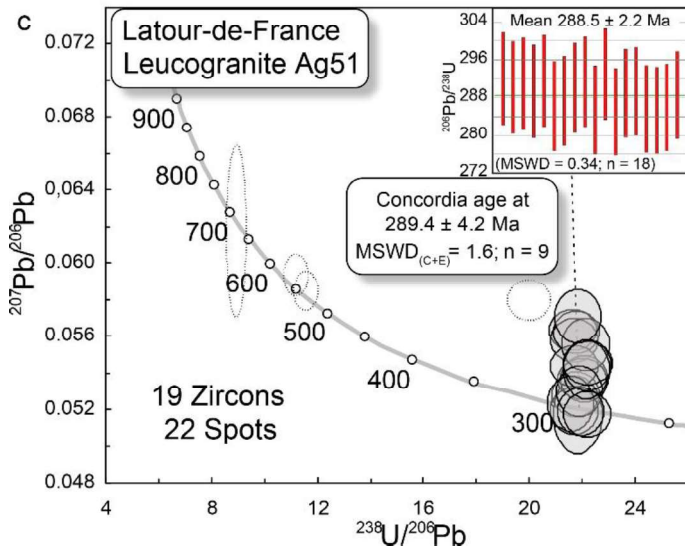
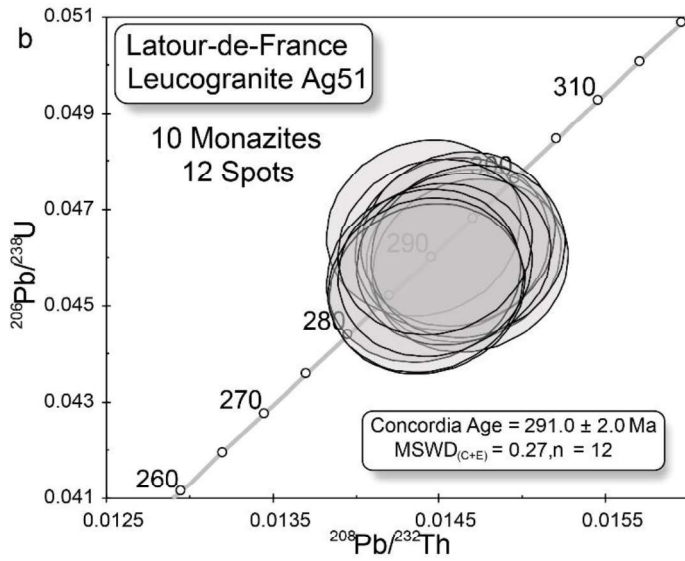
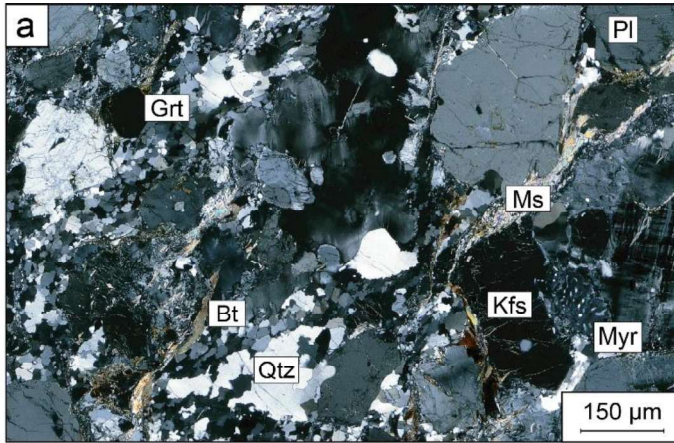
1170

1171 Fig. 12



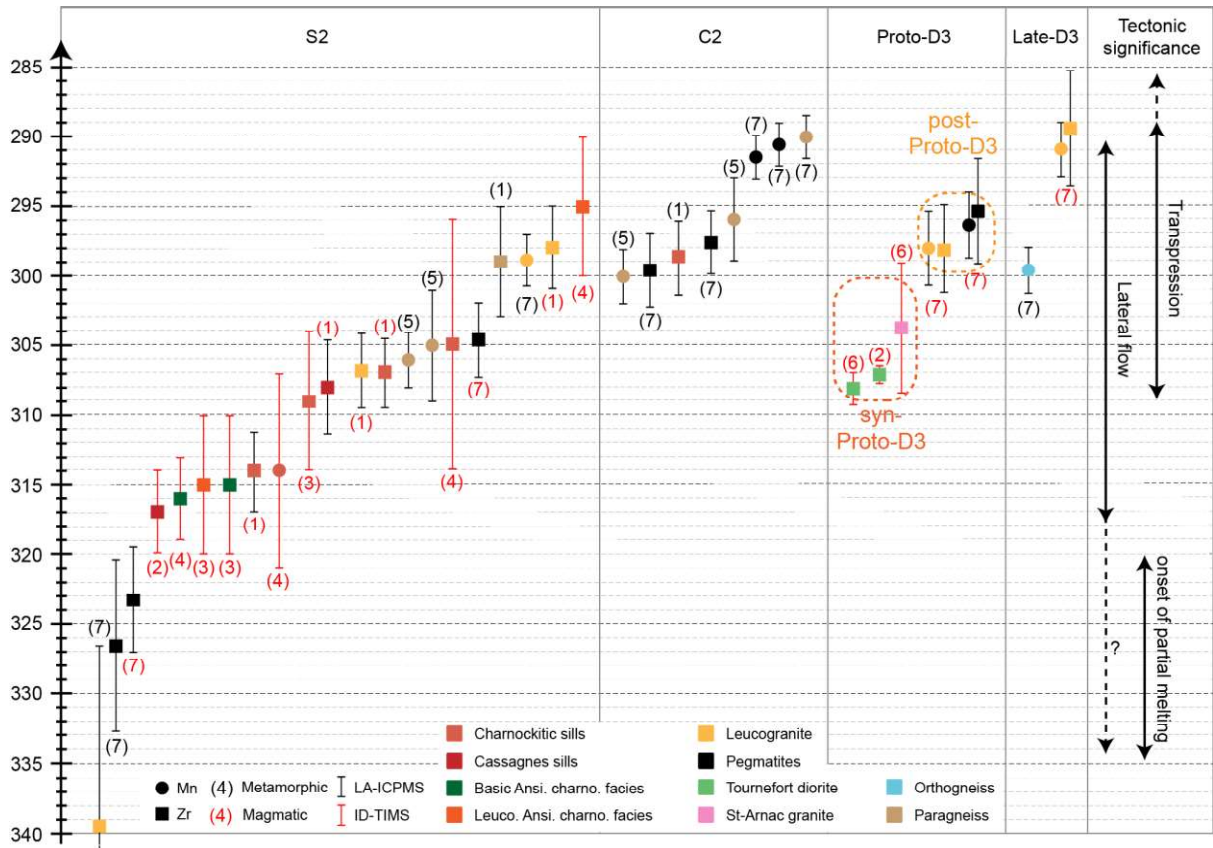
1172

1173 Fig. 13



1174

1175 Fig. 14

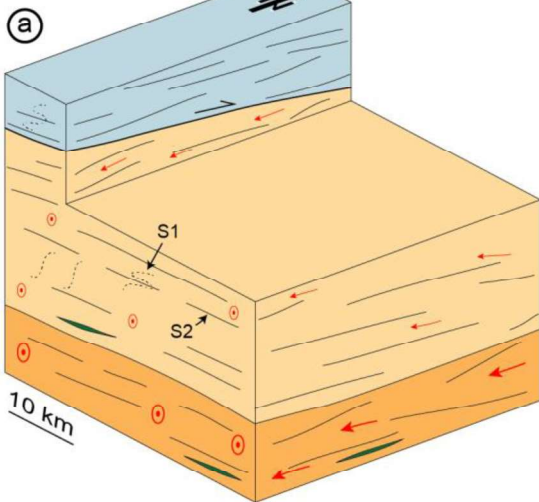


1176

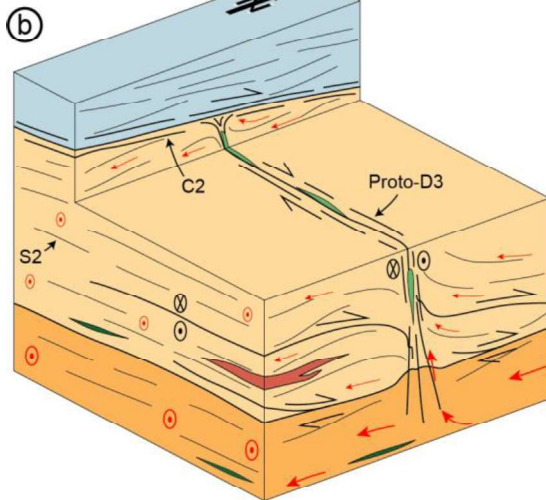
1177 Fig. 15

1178

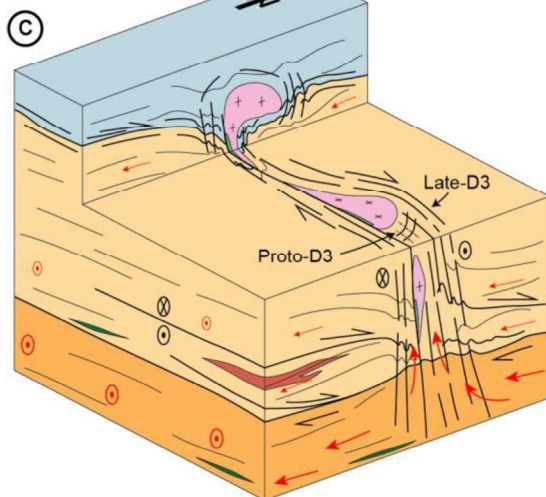
325-308 Ma





308-304 Ma

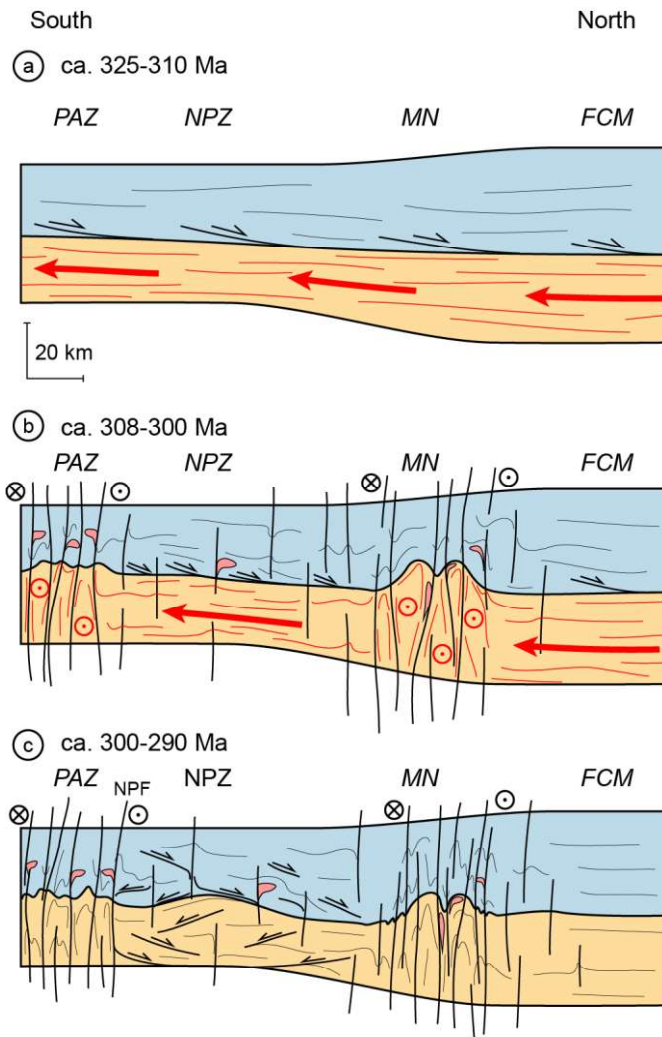


304-300 Ma



- | | |
|---|--|
|  Suprastructure |  Basic sills |
|  Infrastructure |  Ansignan charnockite |
|  Unknown lower crust |  Tournefort diorite |
| |  Saint-Arnac granite |

1180 Fig. 16



1181

1182 Fig. 17

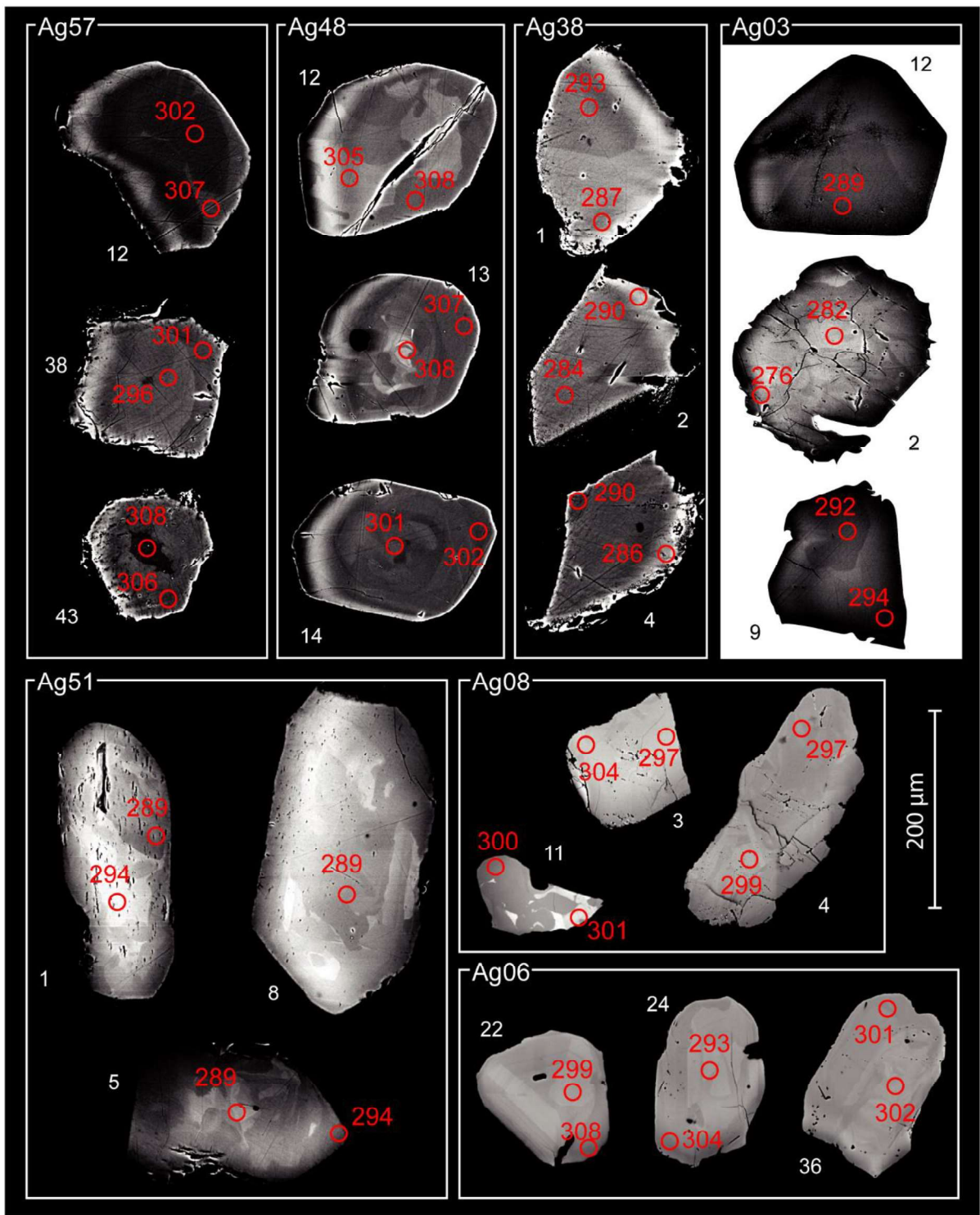
1183

1184 Table 1

Sample	Rock type	Structure	GPS location	U-Th-Pb age ($\pm 2\sigma$)	
				Monazite	Zircon
Samples from S2 strain domains					
Ag57	Vivier deformed leucogranite	Infrastructure	N42°46'07''E02°29'12''	298.9 \pm 1.9 Ma	
				305.8 \pm 6.8 Ma	
				339.5 \pm 13 Ma	
				~ 535 - 620 Ma	
				~ 620 - 730 Ma	
Ag3B (T.S.)	Dam migmatitic paragneiss	Infrastructure	N42°44'51''E02°35'26''	290.2 \pm 1.6 Ma	
Samples from the C2 Shear Zones					
Ag03	Undeformed peg- matite	Suprastructure	N42°44'47''E02°39'44''	290.7 \pm 1.5 Ma	
				304.6 \pm 2.7 Ma	
Ag38	Deformed pegma- tite	Infrastructure	N42°44'47''E02°40'06''	291.5 \pm 1.6 Ma	
				297.6 \pm 2.3 Ma	
Ag47	Planèze mylonitic pegmatite	Suprastructure	N42°46'07''E02°37'16''	299.7 \pm 2.7 Ma	
				527.1 \pm 9.4 Ma	
				326.6 \pm 6.2 Ma	
Samples from the Proto-D3 Tournefort area					
Ag08	Tournefort un- deformed pegma- tite	Suprastructure	N42°45'27''E02°34'12''	296.4 \pm 2.4 Ma	
				295.5 \pm 3.8 Ma	
				323.3 \pm 3.8 Ma	
Ag06	Tournefort un- deformed Leuco- granite	Suprastructure	N42°45'54''E02°34'32''	298.2 \pm 2.7 Ma	
				298.3 \pm 3.2 Ma	
Samples from the Late-D3 Tournefort Deformation Zone					
Ag48	Vivier Orthogneiss	Infrastructure	N42°46'16''E02°28'42''	299.7 \pm 1.7 Ma	
				303.9 \pm 5.5 Ma	

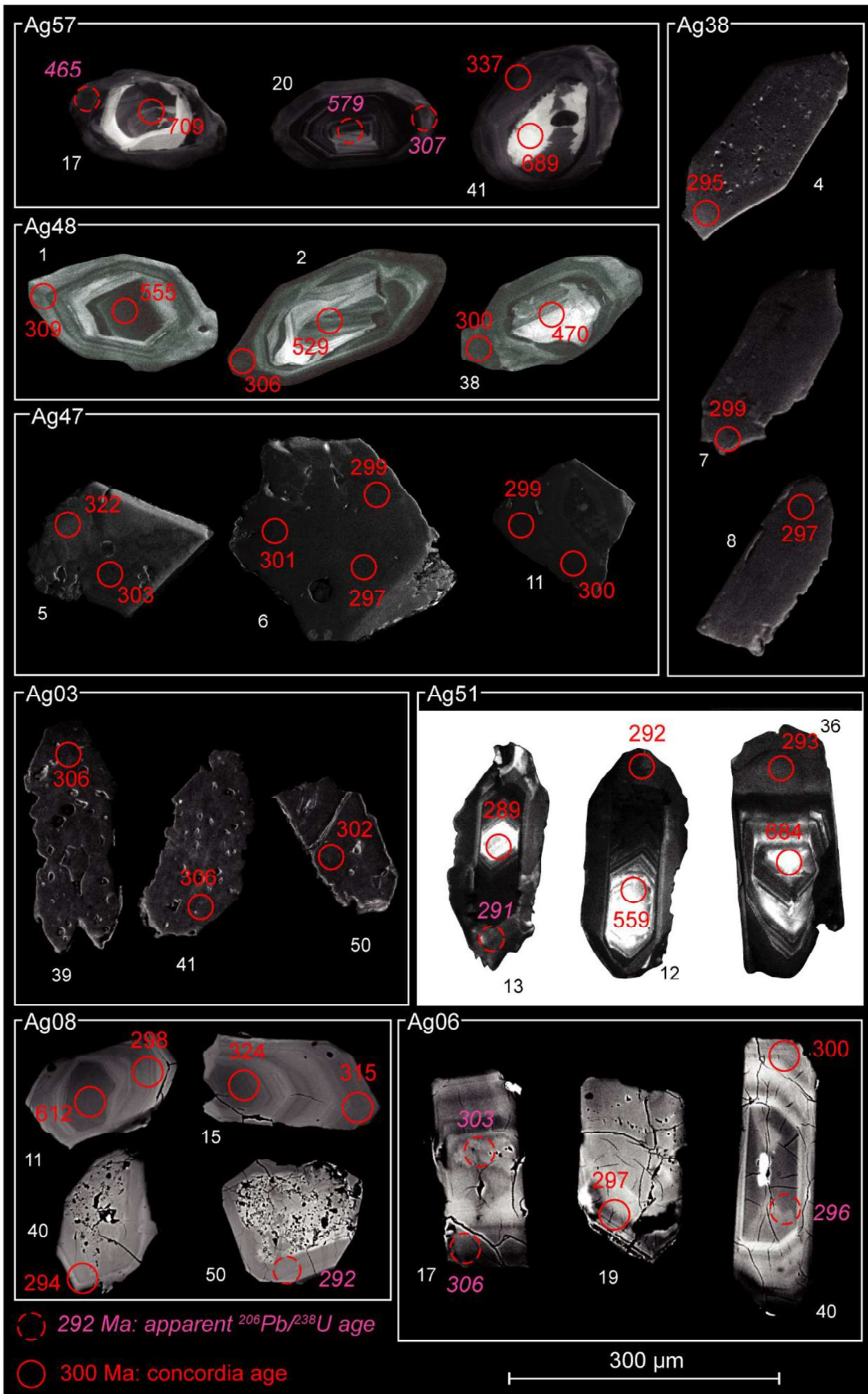
				~ 440 - 480 Ma
				551.8 ± 4.8 Ma
				597.2 ± 7.7 Ma
Ag51	Latour de France	Infrastructure	N42°45'38''E02°38'50''	291 ± 2 Ma
	leucogranite			289.4 ± 4.2 Ma

1185



1186

1187 Fig. S1



1188

1189 Fig. S2